

Role of Perferryl–Oxo Oxidant in Alkane Hydroxylation Catalyzed by Cytochrome P450: A Hybrid Density Functional Study

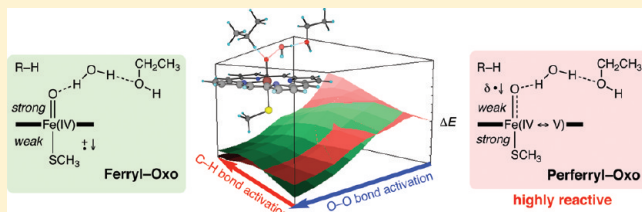
Hiroshi Isobe,*† Kizashi Yamaguchi,† Mitsutaka Okumura,† and Jiro Shimada‡

†Department of Chemistry, Graduate School of Science, Osaka University, Toyonaka, Osaka 560-0043, Japan

‡Green Innovation Research Laboratories, NEC Corporation, 34, Miyukigaoka, Tsukuba, Ibaraki 305-8501, Japan

Supporting Information

ABSTRACT: We have performed hybrid density functional theory (DFT) calculations on the reactivities of low-lying doublet and quartet ferryl–oxo [$\text{Fe(IV)}=\text{O}$] oxidants and a doublet perferryl–oxo [$\text{Fe(V)}=\text{O}$] oxidant as a new key active species in cytochrome P450. Several aspects of the mechanism of hydrogen-atom abstraction from propane by the above active species of compound I models have been addressed in detail. The results, based on fully optimized structures, demonstrate that the perferryl–oxo oxidant can contribute to the reactivity of compound I owing to the presence of a highly reactive $p\pi$ atomic radical character of the oxo ligand. The perferryl–oxo species can abstract a hydrogen atom from propane with an activation barrier of only 0.6–2.5 kcal mol⁻¹, which is substantially smaller than that for the ferryl–oxo species (13.4–17.8 kcal mol⁻¹). The role of the doublet perferryl species in the heterolytic and homolytic O–O bond cleavage in precursor (protonated) compound 0 coupled with the subsequent C–H bond activation has also been explored by grid search of ferryl and perferryl potential surfaces using two parameters. Our calculations suggest that the perferryl–oxo oxidant is catalytically competent, if the O–O bond cleaves heterolytically. The interplay between the accessible ferryl and perferryl states of compound I with quite different reactivities could be a possible reason for elusiveness of compound I in native P450 catalysis on the one hand and various degrees of detection in shunt reactions using peroxy acids on the other hand.

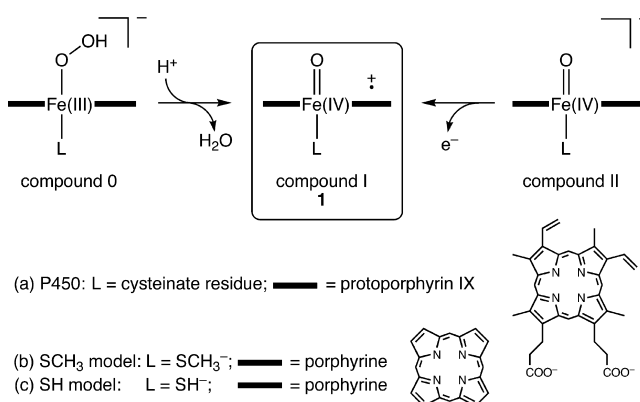


1. INTRODUCTION

Cytochrome P450 (P450) enzymes constitute a super family of ubiquitous metabolizing proteins that perform a wide variety of biological functions in aerobic organisms including the biosynthesis of endogenous compounds such as cholesterol, steroids, and lipids, the catabolism of xenobiotics, and even the activation of carcinogens.¹ The heme prosthetic group, the cofactor within P450 that catalyzes the reductive activation of molecular oxygen (O_2), contains an iron atom as a catalytic agent that is coordinated by four nitrogen atoms of a protoporphyrin IX macrocycle and a cysteinate residue as the proximal ligand, which is responsible for the characteristic Soret absorption maximum of the $\text{Fe(II)}-\text{CO}$ complex at around 450 nm.² It is proposed that a high-valent ferryl–oxo [$\text{Fe(IV)}=\text{O}$] complex with a porphyrin π -cation radical, known also as compound I (1, Chart 1), is generated in the catalytic center with two protons from surrounding solvent and two electrons from NADH or NADPH.^{3,4} This highly oxidized iron–oxo species 1 has generally been assumed to be the primary oxidizing species responsible for the energy-demanding two-electron oxidations of hydrophobic compounds, especially for the hydroxylation of saturated hydrocarbons.^{1,4}

The hydroxylation of unactivated alkanes (RH) by 1 is believed to proceed in a stepwise manner, as shown in Scheme 1, with initial abstraction of a hydrogen atom from the C–H bond of the substrate, $2 \rightarrow \text{TS1} \rightarrow 3$, followed by rapid recombination of the resulting substrate radical ($\text{R}\cdot$) with the

Chart 1



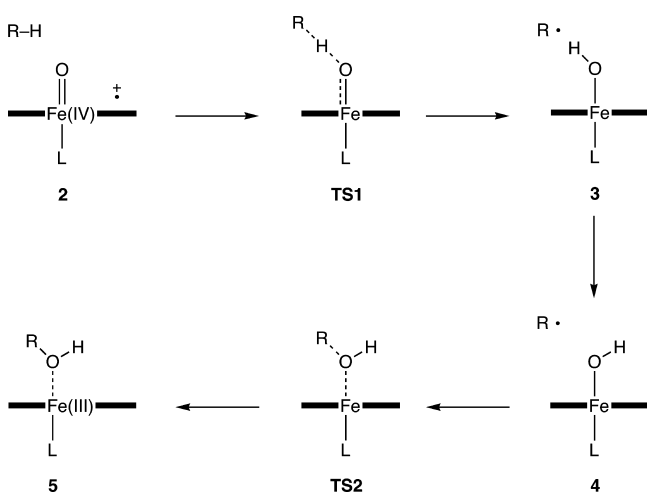
hydroxo ligand to produce a ferric alcohol product, $3 \rightarrow 4 \rightarrow \text{TS2} \rightarrow 5$, which is termed the oxygen rebound mechanism by Groves et al.⁵ Support for this discrete radical mechanism comes from large kinetic isotope effects,^{5b,6} loss of stereochemical configurations,^{5b,c,6b,d} and theoretical calculations.⁷ Despite progress in understanding of the catalytic mechanism, however, several experimental studies have raised intriguing

Received: November 21, 2011

Revised: March 18, 2012

Published: April 17, 2012

Scheme 1



controversies about the identity of the active oxidant in P450-catalyzed reactions, leading to a two-oxidant or multiple-oxidant hypothesis.⁸ On the basis of site-specific mutagenesis studies, a ferric–hydroperoxide [Fe(III)–OOH⁻] precursor, so-called compound 0 (Chart 1), was proposed as a second electrophilic agent that transfers an oxygen atom into C=C double bonds, since mutants, in which proton delivery for the conversion of compound 0 to compound I is blocked, still retained or even enhanced the reactivity toward olefin epoxidation relative to allylic hydroxylation.^{9,10} Further experimental studies, however, showed that compound 0 is far less reactive than compound I.¹¹ Theory also clarified that barriers for epoxidation by compound 0 are much higher than those by compound I because of strong basicity and poor electron-accepting capability for the former.¹² Newcomb and co-workers analyzed kinetics of the rebound step by using a series of radical clock substrates for the determination of rate constants and suggested a cationic OH⁺ insertion pathway involving compound 0 and a nonsynchronous concerted oxygen insertion pathway, in which oxygen radical was assumed to approach a C–H bond in a side-on orientation with a lifetime as short as femtoseconds.^{8a,13} The results of the radical clock experiments were later reinterpreted theoretically in terms of the “two-state reactivity”,^{7b,c,14} which rationalized the apparently conflicting experimental results from ultrafast radical clocks, kinetic isotope effects, and stereochemical scrambling patterns. This scenario assumes the interplay between quartet and doublet states along the reaction pathway, which show similar behavior in the initial hydrogen abstraction step but differ significantly in the subsequent rebound step.^{7b,c,14} A significant barrier is usually required for the radical recombination process in the quartet state, while, in the doublet state, the process is assumed to be almost barrier free. The spin state is, therefore, a discriminating factor in the chemistry of 1, affecting the detectable stereochemical scrambling of products. Newcomb et al. recently applied laser flash photolysis (LFP) to the reactions of peroxynitrite with P450 enzymes to generate compound I by the photooxidation of a ferryl–oxo complex with a closed-shell porphyrin, called compound II (Chart 1), with laser light of 355 nm, and investigated the reactivities of various LFP-generated species.¹⁵ The finding that rate constants for oxidations by the LFP-generated species are much smaller than that for oxidation in the catalytic cycle of P450 led them to suggest that the oxidizing species of P450

could be the perferryl–oxo [Fe(V)=O] precursor.¹⁵ Following these studies, Rittle et al. analyzed the UV–visible spectrum of compound I obtained from the stopped-flow reaction of P450 with *meta*-chloroperoxybenzoic acid (*m*CPBA),¹⁶ which resembled closely the spectrum of compound I^{4a,b} but had no similarity to the LFP-generated spectrum. They concluded from these results that the LFP-generated intermediate is not P450 compound I.¹⁶ Recently, two theoretical papers appeared that predicted that the pentaradicaloid and perferryl states may lie only a few kcal mol⁻¹ above the triradicaloid ground state.¹⁷ These studies arrived at this prediction by QM/MM (CASPT2/MM) calculations on compound I of P450 and chloroperoxidase^{17a} and QM-only [DFT, CASPT2, RASPT2, and CCSD(T)] calculations on heme complexes.^{17b}

The controversies mentioned above arise to a large extent from the fact that compound I has not been detected experimentally during the native catalytic cycle of P450, in which oxygen and redox equivalents are provided from O₂, the most abundant and accessible oxidant, and NAD(P)H via iron–sulfur protein or FAD/FMN-containing flavoprotein.^{1,19} This difficulty, however, can be circumvented by the use of peroxy acid such as *m*CPBA as oxygen and electron source (shunt reaction),^{4a,b,d,16,19} which made it possible to isolate compound I from the thermophilic P450 enzyme CYP119 and has established a ferryl ground state unambiguously.²⁰ To shed light on the origin of the above apparently inconsistent experimental results from the native route using O₂/2H⁺/2e⁻ and its substitute route using peroxy acid, we have addressed the geometric and electronic structures and reactivities of several low-lying ferryl–oxo oxidants of triradical character and a doublet perferryl–oxo oxidant. A previous study has shown that the unique structural and electronic features of the doublet perferryl–oxo oxidant are associated with spin polarization of π electrons within the iron–oxo core with the assistance of electron-pair donation from the basic thiolate ligand to the Fe center.²¹ The resulting terminal oxygen radical has attracted our attention as a candidate for the active oxidant in the P450 catalysis. In this study, we have performed hybrid density functional theory (DFT) calculations on the reactions of the ferryl and perferryl compound I models with unactivated C–H bonds of alkanes to show the extremely high reactivity of the latter species. The behaviors of ferryl and perferryl species in the coupled O–O and C–H bond activation have also been investigated with the hope to identify what mechanistic role the perferryl–oxo oxidant may play. Our calculations suggest that the perferryl–oxo oxidant is catalytically competent, if the O–O bond cleaves heterolytically. We anticipate that the interplay between the accessible ferryl and perferryl states of compound I with quite different reactivities could be a possible reason for elusiveness of compound I in native P450 catalysis on the one hand and various degrees of detection in shunt reactions using peroxy acids on the other hand.

2. COMPUTATIONAL DETAILS AND THEORETICAL BACKGROUNDS

The same chemical models and methods as those adopted previously²¹ have been used for the present study, except for additional test calculations.

2.1. Compound I Models. Compound I was modeled by an iron–oxo porphyrin complex with the side chains of the heme truncated, as indicated in Chart 1. The proximal ligand was represented by either a methylthiolate anion (SCH₃⁻) or a thiolate anion (SH⁻), which we call the SCH₃ and SH models

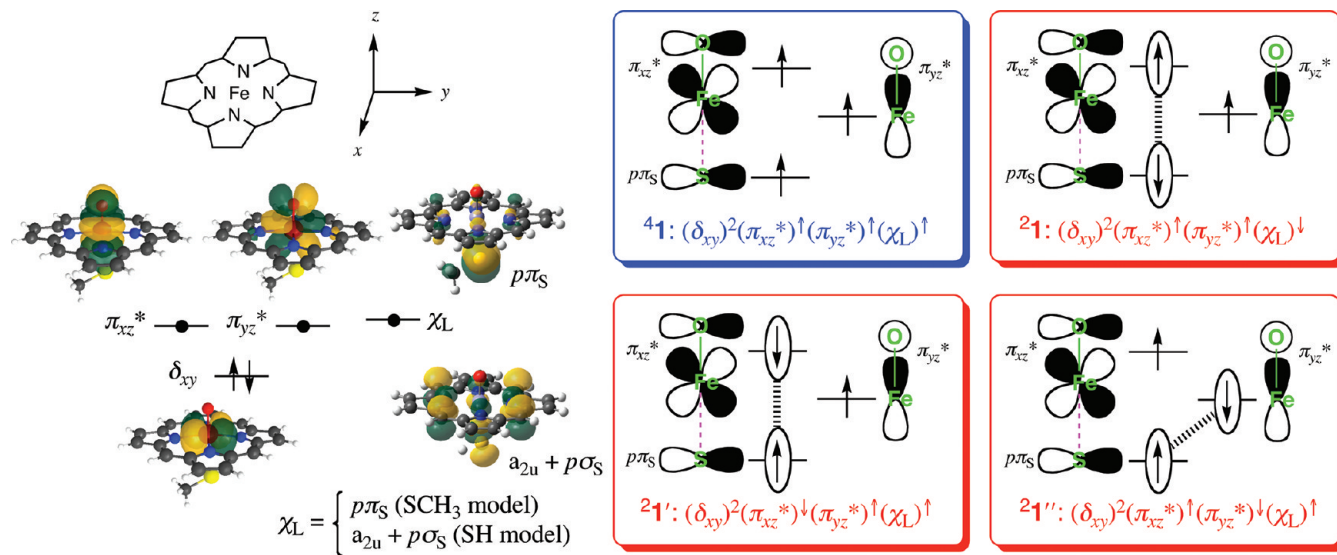


Figure 1. Electronic configurations of ferryl compound I; electrons in formally paired spin-polarized orbitals, ψ_{HONO}^{\pm} (eq 2a), are marked by two ellipses with a hashed line representing a bonding interaction between the two spin-paired electrons in ψ_{HONO}^{\pm} ; note that the $p\sigma_S$ orbital may be mixed with the $p\pi_S$ orbital to generate a tilted hybrid orbital on the sulfur.

throughout this paper; the subscript, SH, is used for the latter to distinguish the two models. Propane ($\text{CH}_3\text{CH}_2\text{CH}_3$, a) was chosen as a prototypical substrate to be oxidized by the above compound I models, except for additional test calculations using a large basis set, for which methane (CH_4 , b) and the SH model oxidant were employed to reduce computational demand.

2.2. Methods. Geometry optimizations of reactants, transition structures (TS), and intermediates were performed using the unrestricted (U) B3LYP method²² with an effective core potential basis set of double- ζ quality (CEP-31G),²³ hereafter denoted by BS1, implemented in Gaussian 03.^{24a} Frequency calculations were carried out with the same basis set to verify the nature of all stationary points and to derive zero-point vibrational corrections (ZPC) without scaling and thermodynamics effects at 298.15 K by statistical mechanics calculations. The final energetics was further evaluated by single-point calculations at each optimized geometry with an extensive all-electron basis set augmented with polarization and diffuse functions on all atoms, i.e., the Wachters (augmented with Bauschlicher f functions) basis set²⁵ on the Fe atom and the 6-31++G(d,p) basis set²⁶ on the C, H, O, N, and S atoms, labeled as BS2. The bulk polarity effect was evaluated by the CPCM-UAKS model²⁷ at the B3LYP/BS2 level. The dielectric constant (ϵ) of 4.0 was employed to represent a protein-like environment. For some important structures, additional optimization and frequency calculations were performed using different types of density functionals [hybrid functional (B3LYP),²² hybrid meta functional (M06),²⁸ and range-separated functionals (CAM-B3LYP,²⁹ HSE06,³⁰ and ω B97X-D³¹)] implemented in Gaussian 09^{24b} combined with the large basis set, BS2.

2.3. Natural Orbital Analysis. To make a theoretical interpretation of the electronic characteristics of optimized structures, symmetry-adapted natural orbitals (ϕ) were determined by diagonalizing the spin-traced first-order density matrices [$\rho(\mathbf{r}', \mathbf{r})$] of broken-symmetry (BS) solutions (canonical Kohn–Sham orbitals $\psi^{\alpha\beta}$ or corresponding orbitals ψ^{\pm}),³² as given by eq 1, in which N^+ and N^- are the numbers of up and down spins satisfying the inequality $N^+ \geq N^-$.

$$\begin{aligned} \rho(\mathbf{r}', \mathbf{r}) &= \sum_{i=1}^{N^+} \psi_i^\alpha(\mathbf{r}') \psi_i^{\alpha*}(\mathbf{r}) + \sum_{i=1}^{N^-} \psi_i^\beta(\mathbf{r}') \psi_i^{\beta*}(\mathbf{r}) \\ &= \sum_{i=1}^{N^-} [n_i \phi_i(\mathbf{r}') \phi_i^*(\mathbf{r}) + n_{-i} \phi_{-i}(\mathbf{r}') \phi_{-i}^*(\mathbf{r})] \\ &\quad + \sum_{i=1}^{N^+ - N^-} \phi_{0,i}(\mathbf{r}') \phi_{0,i}^*(\mathbf{r}) \end{aligned} \quad (1)$$

The natural orbitals (ϕ) can be transformed into corresponding orbitals (ψ^{\pm}),³³ as shown in eq 2, in which ω_i is the orbital mixing angle ($0 \leq \omega_i \leq \pi/2$).

$$\psi_i^{\pm}(\mathbf{r}) = \cos \omega_i \phi_i(\mathbf{r}) \pm \sin \omega_i \phi_{-i}(\mathbf{r}) \quad (2a)$$

$$\psi_{0,i}^+(\mathbf{r}) = \phi_{0,i}(\mathbf{r}) \quad (2b)$$

The eigenvalues, $n_{\pm i}$ and 1, can be interpreted as the occupation numbers of the natural orbitals, $\phi_{\pm i}$ and $\phi_{0,i}$, and used to extract important orbitals that characterize the electronic property of the reacting system under investigation. In a doublet triradical system like compound I ($N^+ - N^- = 1$), there should be three natural orbitals with an occupation number close to 1.0. One of them arises from eq 2b and has an exactly single occupancy, which we call below SONO (singly occupied natural orbital, ϕ_{SONO}), while the other two originate from eq 2a and make a pair with fractional occupation numbers, $1 \pm \langle \psi_{\text{HONO}}^+ | \psi_{\text{HONO}}^- \rangle$, which we call HONO (highest occupied natural orbital, ψ_{HONO}) and LUNO (lowest unoccupied natural orbital, ψ_{LUNO}). The orbital overlap integral between the corresponding orbitals $\psi_{\text{HONO}}^{\pm}(T)$, which is related with the occupation number of HONO by eq 3, can be chosen as a measure of the extent of bonding interaction between formally paired electrons in ψ_{HONO}^{\pm} .

$$T \equiv \langle \psi_{\text{HONO}}^+ | \psi_{\text{HONO}}^- \rangle = \cos 2\omega_{\text{HONO}} = n_{\text{HONO}} - 1 \quad (3)$$

All active orbitals (HONO, LUNO, and SONO) and their occupation numbers, as well as Mulliken charge and spin

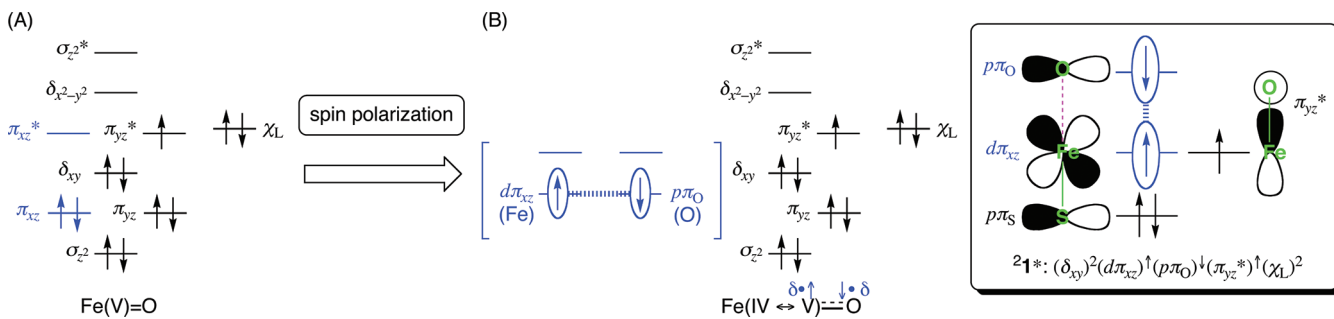


Figure 2. Electronic configurations of perferryl compound I: (A) formal orbital picture and (B) actual orbital picture, in which an up-spin electron and its formally paired down-spin counterpart in the bonding π_{xz} orbital occupy partially different regions of space, as highlighted in blue.

populations, for structures reported in this paper are available as Supporting Information.

3. RESULTS AND DISCUSSION

3.1. Electronic Structures of Compound I. In this study, we have addressed the reactivities of four ferryl–oxo configurations of triradical character ($^4\mathbf{1}$, $^2\mathbf{1}$, $^2\mathbf{1}'$, and $^2\mathbf{1}''$) and a doublet perferryl–oxo configuration ($^2\mathbf{1}^*$), whose orbital occupancies and bonding patterns are defined in Figures 1 and 2.

3.1.1. Ferryl–Oxo Species. In the ferryl compound I, there are three low-lying valence orbitals or hybrid orbitals available to three unpaired electrons, as depicted in Figure 1. Three electrons can choose from two antibonding π^* orbitals of the iron–oxo core and one ligand-based orbital (χ_L), which is either a sulfur $p\pi_S$ orbital (SCH₃ model) or a porphyrin a_{2u} orbital mixed with a sulfur $p\sigma_S$ orbital (SH model).⁷ The ground electronic configurations of the ferryl–oxo oxidant are $^4\mathbf{1}$ and $^2\mathbf{1}$ with “local triplet”³⁴ coupling between two electrons in the orthogonal π_{xz}^* and π_{yz}^* orbitals, which are nearly degenerate in energy to within 1 kcal mol⁻¹. $^2\mathbf{1}'$ and $^2\mathbf{1}''$ also make a degenerate pair of excited electronic configurations with “local singlet”³⁴ coupling, which lies about 8–9 kcal mol⁻¹ above $^4\mathbf{1}$ and $^2\mathbf{1}$, as required by Hund’s rule. Three configurations with $S_z = 1/2$, $^2\mathbf{1}$, $^2\mathbf{1}'$, and $^2\mathbf{1}''$, are, however, not eigenstates of the $\hat{\mathbf{S}}^2$ operator but can be used to build three correct spin-adapted states. In addition to one quartet state described as $(\delta_{xy})^2[(\pi_{xz}^*)^\dagger(\pi_{yz}^*)^\dagger(\chi_L)^\downarrow + (\pi_{xz}^*)^\dagger(\pi_{yz}^*)^\dagger(\chi_L)^\uparrow + (\pi_{xz}^*)^\dagger(\pi_{yz}^*)^\dagger(\chi_L)^\uparrow]$, the remaining two doublet states conform to the following representations:

$$(^2\mathbf{1}' \leftrightarrow ^2\mathbf{1}'')_T: (\delta_{xy})^2[2(\pi_{xz}^*)^\dagger(\pi_{yz}^*)^\dagger(\chi_L)^\downarrow - (\pi_{xz}^*)^\dagger(\pi_{yz}^*)^\dagger(\chi_L)^\uparrow - (\pi_{xz}^*)^\dagger(\pi_{yz}^*)^\dagger(\chi_L)^\uparrow]$$

$$(^2\mathbf{1}' \leftrightarrow ^2\mathbf{1}'')_S: (\delta_{xy})^2[(\pi_{xz}^*)^\dagger(\pi_{yz}^*)^\dagger(\chi_L)^\uparrow - (\pi_{xz}^*)^\dagger(\pi_{yz}^*)^\dagger(\chi_L)^\uparrow]$$

We denote these doublet states by $(^2\mathbf{1}' \leftrightarrow ^2\mathbf{1}'')_T$ and $(^2\mathbf{1}' \leftrightarrow ^2\mathbf{1}'')_S$, since these two states result from resonance between spin-projected $^2\mathbf{1}'$ and $^2\mathbf{1}''$.²¹ The subscripts T and S indicate that the ferryl–oxo subunit is characterized by pure local triplet and singlet states. In this study, we have used the term “configuration” for DFT-optimized structures ($^2\mathbf{1}$, $^2\mathbf{1}'$, $^2\mathbf{1}''$, and so on), which are, in most cases, different from real states [$(^2\mathbf{1}' \leftrightarrow ^2\mathbf{1}'')_T$, $(^2\mathbf{1}' \leftrightarrow ^2\mathbf{1}'')_S$, and so on].

The approximate spin projection (AP) scheme³⁵ can be used to estimate the total energy of $(^2\mathbf{1}' \leftrightarrow ^2\mathbf{1}'')_T$ by projecting the $^2\mathbf{1}$ configuration onto a doublet state, as given by eq 4, in which

xE_{BS} and ${}^X\langle \hat{\mathbf{S}}^2 \rangle_{\text{BS}}$ stand for the total energy and the expectation value of the spin operator $\hat{\mathbf{S}}^2$ taken with respect to the BS wave function for the spin multiplicity X .

$$\begin{aligned} {}^2E(^2\mathbf{1}' \leftrightarrow ^2\mathbf{1}'')_T &= {}^2E(\text{spin-projected } ^2\mathbf{1}) \sim {}^2E_{\text{AP}}(^2\mathbf{1}) \\ &= {}^2E_{\text{BS}}(^2\mathbf{1}) + \frac{{}^2\langle \hat{\mathbf{S}}^2 \rangle_{\text{BS}} - 0.75}{{}^4\langle \hat{\mathbf{S}}^2 \rangle_{\text{BS}} - {}^2\langle \hat{\mathbf{S}}^2 \rangle_{\text{BS}}} \\ &\quad \times [{}^2E_{\text{BS}}(^2\mathbf{1}) - {}^4E_{\text{BS}}(^4\mathbf{1})] \end{aligned} \quad (4)$$

The AP scheme is, however, problematic with respect to the degenerate $^2\mathbf{1}'$ and $^2\mathbf{1}''$ configurations because of linear dependency among spin-projected $^2\mathbf{1}$, $^2\mathbf{1}'$, and $^2\mathbf{1}''$. We have made use of Löwdin’s projection³⁶ to resolve the linear dependency and to obtain the approximate total energy of $(^2\mathbf{1}' \leftrightarrow ^2\mathbf{1}'')_S$ that is orthogonal to $(^2\mathbf{1}' \leftrightarrow ^2\mathbf{1}'')_T$, as indicated in eq 5, by a procedure described in detail in a previous paper.²¹

$$\begin{aligned} {}^2E(^2\mathbf{1}' \leftrightarrow ^2\mathbf{1}'')_S &\sim (2/3)[{}^2E_{\text{AP}}(^2\mathbf{1}') + {}^2E_{\text{AP}}(^2\mathbf{1}'')] \\ &\quad - {}^2E_{\text{AP}}(^2\mathbf{1})/3 \end{aligned} \quad (5)$$

$(^2\mathbf{1}' \leftrightarrow ^2\mathbf{1}'')_T$ and $(^2\mathbf{1}' \leftrightarrow ^2\mathbf{1}'')_S$ are no longer degenerate, with the former energetically preferred by about 18 kcal mol⁻¹. Equations 4 and 5 are also valid for the loosely bound reactant complex, 2. A similar procedure can in principle be applied to the loosely bound radical intermediate complex, 3, but in this case has little effect on its energy, as mentioned later.

3.1.2. Perferryl–Oxo Species. The electronic configuration of the doublet perferryl–oxo oxidant can be formally expressed as shown in Figure 2A; one electron resides in the antibonding π_{yz}^* orbital of the iron–oxo core and two electrons are paired in the ligand-based orbital. Thus, the perferryl–oxo species appears as a monoradical. However, significant electron repulsion between electrons that occupy the bonding π_{xz} orbital causes important modifications to this formal orbital picture; the delocalized π_{xz} orbital now splits into two localized $d\pi_{xz}$ and $p\pi_O$ orbitals for its up and down spins by admixing some antibonding π character from the empty π_{xz}^* orbital, as shown in Figure 2B, thereby leaving behind an unpaired electron effectively contracted on the terminal oxo group.²¹ The $d\pi_{xz}$ and $p\pi_O$ orbitals span in the same xz plane and can partially overlap with $T = 0.35$. The doublet perferryl species should, therefore, be in a mixed Fe(IV)–Fe(V) state and lie much lower in energy than the corresponding quartet perferryl species, for which such overlap is forbidden at the equilibrium geometry of the doublet state. Since the BS wave function of $^2\mathbf{1}^*$ contains higher-lying high-spin components as a result of the mixing, its energy (ca. 8.8–13.5 kcal mol⁻¹ relative to $^4\mathbf{1}$)

Table 1. Relative Energies, Bond Lengths, Bond Stretching Frequencies, and Mulliken Spin Densities for Ferryl and Perferryl Configurations of Compound I (SH Model, 1_{SH}) at the Various Levels of Theory

species	$\Delta E + \text{ZPC}^a$	bond length ^b		frequency ^c		Mulliken spin density			
		r_{FeO}	r_{FeS}	ν_{FeO}	ν_{FeS}	Fe	O	SH	porphyrin
B3LYP/BS1//BS1									
${}^2\mathbf{1}_{\text{SH}}$	0.0	1.650	2.631	884.1	145.9	1.21	0.91	-0.61	-0.52
${}^2\mathbf{1}_{\text{SH}}^*$	8.8	1.782	2.352	566.7	302.7	1.90	-0.84	0.14	-0.20
B3LYP/BS2//BS2									
${}^2\mathbf{1}_{\text{SH}}$	-0.2	1.631	2.572	886.0	152.3	1.26	0.84	-0.60	-0.51
${}^2\mathbf{1}_{\text{SH}}^*$	10.3	1.737	2.295	550.0	315.9	1.64	-0.70	0.23	-0.17
CAM-B3LYP/BS2//BS2									
${}^2\mathbf{1}_{\text{SH}}$	-0.1	1.605	2.606	955.5	132.4	1.23	0.86	-0.75	-0.35
${}^2\mathbf{1}_{\text{SH}}^*$	11.3	1.742	2.262	588.9	326.5	1.75	-0.76	0.16	-0.15
HSE06/BS2//BS2									
${}^2\mathbf{1}_{\text{SH}}$	-0.2	1.617	2.510	915.2	177.3	1.28	0.84	-0.65	-0.47
${}^2\mathbf{1}_{\text{SH}}^*$	7.3	1.746	2.267	576.2	327.9	1.77	-0.77	0.18	-0.18
M06/BS2//BS2									
${}^2\mathbf{1}_{\text{SH}}$	-0.8	1.628	2.505	894.1	185.7	1.19	0.79	-0.59	-0.40
${}^2\mathbf{1}_{\text{SH}}^*$	6.4	1.761	2.287	555.6	317.6	1.81	-0.83	0.10	-0.07
$\omega\text{B97X-D}/\text{BS2}/\text{BS2}$									
${}^2\mathbf{1}_{\text{SH}}$	0.0	1.610	2.565	949.4	140.8	1.22	0.86	-0.67	-0.41
${}^2\mathbf{1}_{\text{SH}}^*$	11.5	1.740	2.259	575.9	336.0	1.68	-0.76	0.20	-0.12

^aRelative energies including ZPC with respect to the ${}^4\mathbf{1}_{\text{SH}}$ configuration are given in kcal mol⁻¹. ^bFe–O (r_{FeO}) and Fe–S (r_{FeS}) bond lengths are given in angstroms. ^cUnscaled stretching frequencies of Fe–O (ν_{FeO}) and Fe–S (ν_{FeS}) bonds are given in cm⁻¹.

can be regarded as an upper bound to that of the spin-adapted mixed-valent state.

3.1.3. Effects of Basis Sets and Functionals. To examine the dependence of the geometries and energetics of compound I on basis sets and functionals, we have performed full optimizations of several ferryl and perferryl configurations of the SH model (${}^4\mathbf{1}_{\text{SH}}$, ${}^2\mathbf{1}_{\text{SH}}$, ${}^2\mathbf{1}_{\text{SH}}^*$, and ${}^2\mathbf{1}_{\text{SH}}^{**}$) using five functionals of various types (B3LYP, CAM-B3LYP, HSE06, M06, and $\omega\text{B97X-D}$) in combination with the large basis set BS2, as well as B3LYP/BS1. To highlight the differences between the ferryl and perferryl species, results for ${}^2\mathbf{1}_{\text{SH}}$ and ${}^2\mathbf{1}_{\text{SH}}^*$ are compared in Table 1; a full set of results including ${}^4\mathbf{1}_{\text{SH}}$ and ${}^2\mathbf{1}_{\text{SH}}^{**}$ is given in Table S1 in the Supporting Information. The B3LYP/BS1 method predicts the perferryl species, ${}^2\mathbf{1}_{\text{SH}}^*$, to be 8.8 kcal mol⁻¹ above the ferryl species, ${}^2\mathbf{1}_{\text{SH}}$. Changing the basis set from small BS1 to large BS2 slightly enlarges the ferryl–perferryl adiabatic energy gap by 1.7 kcal mol⁻¹. When the long-range correction is applied through the coulomb-attenuating method (CAM), the energy gap increases further from 10.5 (B3LYP) to 11.4 (CAM-B3LYP) kcal mol⁻¹, which is close to the value for another long-range corrected functional, $\omega\text{B97X-D}$ (11.5 kcal mol⁻¹). On the other hand, the screened functional, HSE06, narrows the energy separation to 7.3 kcal mol⁻¹. The smallest energy gap of 7.2 kcal mol⁻¹ is obtained with the hybrid meta functional, M06. These results indicate that the size of the ferryl–perferryl energy separation is sensitive to the functional, in accordance with previous calculations.^{17b}

Even more important than the quantitative results are the qualitative insights into the underlying electronic features that lead to distinctive structural differences between the ferryl and perferryl species, which are captured by all basis sets and functionals examined; compare results for Fe–O (r_{FeO}) and Fe–S (r_{FeS}) bond lengths, Fe–O (ν_{FeO}) and Fe–S (ν_{FeS}) stretching frequencies, and spin populations in Table 1. The perferryl–oxo species has a longer and weaker Fe–O bond ($r_{\text{FeO}} = 1.74\text{--}1.78 \text{ \AA}$, $\nu_{\text{FeO}} = 550\text{--}589 \text{ cm}^{-1}$) and a shorter and

stronger Fe–S bond ($r_{\text{FeS}} = 2.26\text{--}2.35 \text{ \AA}$, $\nu_{\text{FeS}} = 303\text{--}336 \text{ cm}^{-1}$) than the ferryl–oxo species ($r_{\text{FeO}} = 1.61\text{--}1.65 \text{ \AA}$, $\nu_{\text{FeO}} = 884\text{--}956 \text{ cm}^{-1}$, $r_{\text{FeS}} = 2.51\text{--}2.63 \text{ \AA}$, $\nu_{\text{FeS}} = 132\text{--}186 \text{ cm}^{-1}$). Asymmetric bond length distortion along the O–Fe–S axis mediates the localization of an unpaired electron into different parts, leading to a ligand-based radical for ferryl and a $p\pi_{\text{O}}$ atomic oxygen radical for perferryl. We previously rationalized this phenomenon by formally decomposing the ferryl → perferryl electronic reorganization into the electron transfer and spin polarization processes.²¹ These intrinsically coupled structural and electronic features are decisive for the reactivities of the ferryl and perferryl species, as we shall explore more fully in the following sections.

3.2. Hydrogen Abstraction from Propane by Compound I. Since naked ${}^{1,3}\text{Fe(IV)}=\text{O}$ ions are isoelectronic with ${}^{1,3}\text{O}_2$ ^{35a,37} they are expected to have similar physical and chemical properties. This analogy, however, does not necessarily apply to the case in which the ferryl–oxo core is embedded in the thiolate-ligated porphyrin radical system to form a three-spin system, compound I 1. In fact, a certain fraction of its doublet state is characterized by the local triplet state, (${}^2\mathbf{1}' \leftrightarrow {}^2\mathbf{1}''_{\text{T}}$), and the remaining by the local singlet state, (${}^2\mathbf{1}' \leftrightarrow {}^2\mathbf{1}''_{\text{S}}$), since any superposed state of (${}^2\mathbf{1}' \leftrightarrow {}^2\mathbf{1}''_{\text{T}}$) and (${}^2\mathbf{1}' \leftrightarrow {}^2\mathbf{1}''_{\text{S}}$) is also a doublet state of triradical character. Moreover, not only the quartet state of triradical character but also the highly oxidized perferryl state of some ionic character and several high and intermediate spin states of pentaradical character^{17,18} (not covered in this study) may be allowed to interact with the above two doublet states during the C–H bond activation. These considerations imply that the chemistry of 1 seems to be much more complicated than we might anticipate from ${}^{1,3}\text{O}_2$ reactions. In relation to the perferryl species, it will be useful to classify the behaviors of 1 by the extent of the covalent–ionic interaction, which, for the SCH_3 model, depends on whether there will be any mixing between the $d\pi_{xz}$ orbital on the Fe atom and the adjacent $p\pi_{\text{S}}$ orbital on

the S atom. In this respect, the SCH_3 model has the merit of exhibiting clearly two extreme cases in the orbital mixing arising from the π -bonding interaction between the ferryl–oxo core and the ligand, while this may not be the case in the SH model or in a more realistic model. As a concrete illustration, let us consider specifically the individual behaviors of four ferryl–oxo species, ^4I , ^2I , $^2\text{I}'$, and $^2\text{I}''$ (Figure 1), and one perferryl–oxo species, $^2\text{I}^*$ (Figure 2), for the secondary hydrogen-atom abstraction from propane (**a**) by **1**, separating two parts: the first one dealing with the case in which we expect significant $d\pi-p\pi$ interaction between the ferryl–oxo core and the ligand and the second one focusing on a less favorable case for the interaction. In the following, we shall discuss the issue mainly based on the SCH_3 model and make supplementary remarks on the SH model.

3.2.1. SCH_3 Model: Case I. The energy profiles originating from the above five configurations of compound **I** along the hydrogen-abstraction reaction for the SCH_3 model are given in Figure 3 (BS1) and Figure S1A in the Supporting Information

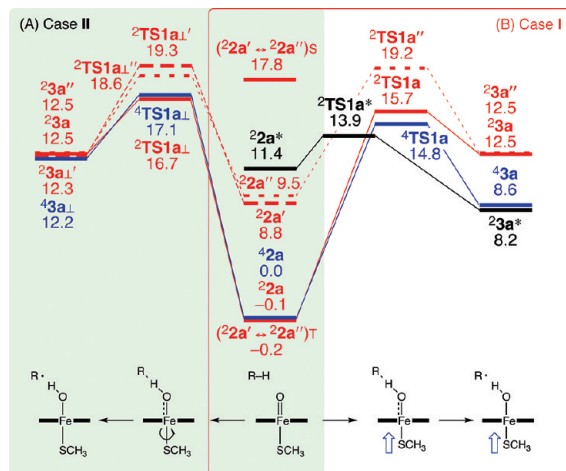


Figure 3. Energy profiles for the secondary hydrogen-atom abstraction from propane by compound **I** (SCH_3 model, **1**) at the B3LYP/BS1 level; relative energies including ZPC are given in kcal mol^{-1} ; the relative energies of $^4\text{a}_\perp$ and $^2\text{a}_\perp'$ were evaluated by single-point calculations using the optimized geometry of ^2a , since minimization searches failed to locate $^4\text{a}_\perp$ and $^2\text{a}_\perp'$ due to the presence of lower-lying ^4a and $^2\text{a}^*$; blue arrows represent the trans effect for $^2\text{a}^*$, $^2\text{TS1a}^*$, $^2\text{3a}^*$, $^4\text{TS1a}$, and $^4\text{3a}$; an arrowhead circle indicates the rotation about the Fe–S bond so as to realize the symmetry-orthogonal relation between the $d\pi_{xz}$ and $p\pi_S$ orbitals at TS1a_\perp .

(BS2//BS1). We adopt the quartet reactant complex, $^4\text{2a}$, as a reference structure for computing relative energies. Figure 4 displays key geometrical parameters of loosely bound reactant complexes between **1** and propane (**2a**), transition structures (**TS1a**), and loosely bound intermediate complexes (**3a**). Their charge and spin density distributions with BS1 and BS2 are collected in Tables S2–S4 in the Supporting Information. The profiles are divided into two cases, depending on the relative orientation of the $p\pi_S$ orbital on the S atom with respect to the adjacent $d\pi_{xz}$ orbital on the Fe atom at **TS1a**. In the first case, the SCH_3 ligand is appropriately orientated so as to attain a large overlap between the $d\pi_{xz}$ and $p\pi_S$ orbitals, and consequently, the electronic reorganization from the ferryl ($^2\text{2a}$) to perferryl ($^2\text{2a}^*$) species is allowed to occur during the reaction. This situation is referred to as case I in Figure 3. Case II is concerned with a less favorable orientation for the ligand—

heme interaction at **TS1a**, for which we expect that electronic reorganization may not occur due to the symmetry-orthogonal relation between the $d\pi_{xz}$ and $p\pi_S$ orbitals. This feature can be verified by the nodal properties of HONO and LUNO of **TS1a** and is symbolized by the subscript “ \perp ” as TS1a_\perp .³⁸

In case I (Figure 3B), the migration of a hydrogen atom from the substrate to the oxo ligand of **1** proceeds with the interchange of pairwise-degenerate ground (G) and excited (E) configurations: $\{^4\text{2a}, ^2\text{2a}\}_G \{^2\text{2a}', ^2\text{2a}''\}_E \rightarrow \{^4\text{3a}, ^2\text{3a}^*\}_G, \{^2\text{3a}, ^2\text{3a}''\}_E$. The reaction lifts the near degeneracy of the pair of the ground configurations of the ferryl–oxo [$\text{Fe(IV)}-\text{O}$] complex, $\{^4\text{2a}, ^2\text{2a}\}_G$, stabilizing the quartet $^4\text{2a}$ relative to the doublet $^2\text{2a}$ by 0.9 (1.8) kcal mol^{-1} for transition structures (TSs), $^4\text{TS1a}$ and $^2\text{TS1a}$, and by 3.9 (4.9) kcal mol^{-1} for intermediate complexes, $^4\text{3a}$ and $^2\text{3a}$, with BS1 (BS2). The quartet configuration originating from $^4\text{2a}$ finally pairs with $^2\text{3a}^*$ in the degenerate ground configurations of the ferryl–hydroxo complex [$\text{Fe(IV)}-\text{OH}$], $\{^4\text{3a}, ^2\text{3a}^*\}_G$. On the other hand, the doublet configuration related to $^2\text{2a}$ rises up along the reaction pathway to make a degenerate pair with $^2\text{3a}''$ in the excited configurations of the ferric–hydroxo complex [$\text{Fe(III)}-\text{OH}$], $\{^2\text{3a}, ^2\text{3a}''\}_E$. At first glance, one might consider $^2\text{TS1a}^*$ and $^2\text{3a}^*$, which lies lowest in energy in the region of TS and intermediate, as arising from the conceptual species, $^2\text{2a}'$. This may be the case at the “configuration” level. In fact, any attempts to search $^2\text{TS1a}'$ and $^2\text{3a}'$ (ferric–hydroxo) using the wave function for $^2\text{2a}'$ (ferryl–oxo) almost always converged to solutions of the lower-lying $^2\text{TS1a}^*$ and $^2\text{3a}^*$ (ferryl–hydroxo) with spontaneous electronic relaxation. This inference is, however, not correct at the “state” level, since $^2\text{2a}'$ and $^2\text{2a}''$ contain a local triplet component of the FeO subunit, as well as a quartet component of the entire system, that lower their energies significantly.²¹ Once AP corrections are made for the energies of $^2\text{2a}'$ and $^2\text{2a}''$ by eq 5, the energy necessary to reach the resonance state for the local singlet ferryl–oxo core, $(^2\text{2a}' \leftrightarrow ^2\text{2a}'')_S$, is calculated to be about 17.8 (18.4) kcal mol^{-1} with BS1 (BS2), which is almost twice as high as $^2\text{2a}'$ and $^2\text{2a}''$, as indicated in Figure 3. It follows that the $(^2\text{2a}' \leftrightarrow ^2\text{2a}'')_S$ state of such high energy is unlikely to have any significance on the chemistry of compound **I** under reasonable conditions. It is the perferryl–oxo species, $^2\text{2a}^*$, that intercepts the pair of the ground configurations of the ferryl–oxo species $\{^4\text{2a}, ^2\text{2a}\}_G$ and eventually becomes a counterpart of the degenerate ground configurations of the radical intermediate, $^2\text{3a}^*$. It should be noted that, unlike the case of $^2\text{2a}'$ and $^2\text{2a}''$, the energy of the $^2\text{2a}^*$ configuration obtained with the BS approach can be regarded as an upper limit to that of the spin-adapted mixed-valent state. Thus, the perferryl–oxo species $^2\text{2a}^*$ can participate in the reaction even at the “state” level.

Several remarks should be made about the energy profiles in case I. In Figure 3B, we connect several TSs to reactants and intermediates by lines, according to the intrinsic reaction coordinate (IRC),³⁹ as shown in Figure S2 in the Supporting Information. The IRC path starting from $^4\text{TS1a}$ leads to the $^4\text{2a}$ and $^4\text{3a}$ configurations; therefore, the lowest-lying quartet ferryl–hydroxo species $^4\text{3a}$ can be understood to be the ferryl–oxo species in origin, even though $^4\text{TS1a}$ has mixed ferryl/perferryl electronic characteristics. On the contrary, the IRC paths from the two doublet TSs, $^2\text{TS1a}$ and $^2\text{TS1a}^*$, remain on diabatic surfaces and cross. We can interpret from the IRC results that the lowest-lying doublet ferryl–hydroxo species $^2\text{3a}^*$ originates from the perferryl–oxo species $^2\text{2a}^*$ via $^2\text{TS1a}^*$

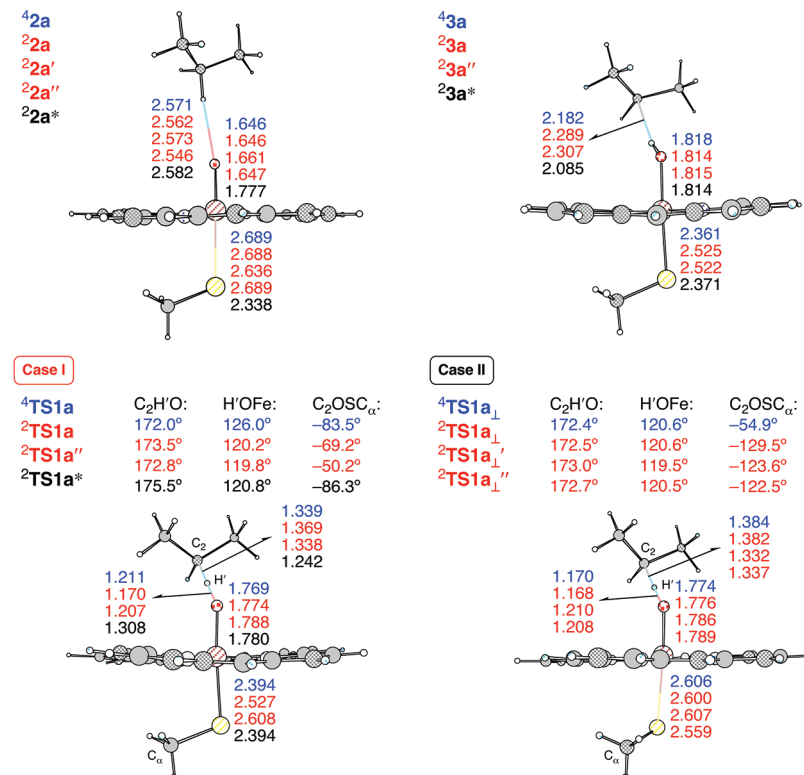


Figure 4. Geometrical parameters of reactant complexes ($2a$), transition structures ($TS1a$), and intermediate complexes ($3a$) for the secondary hydrogen-atom abstraction from propane by compound I (SCH_3 model, 1) at the B3LYP/BS1 level; bond lengths are given in angstroms.

and the higher-lying ferric–hydroxo species 23a from the ferryl–oxo species 22a via 2TS1a . This view will be valid only if the Hamiltonian matrix element between the ferryl and perferryl configurations is small. On the opposite extreme, if the matrix element is significant in the region in which ferryl and perferryl surfaces come close, the ferryl–hydroxo species $^23a^*$ can be better interpreted as having its origin in the ferryl–oxo species 22a , since any pair of energy levels connected by strong interaction does not cross and the ground surface leads smoothly from the ferryl–oxo reactant to the ferryl–hydroxo intermediate via a lower-lying doublet TS (Figure S2D, Supporting Information).⁴⁰ In such a situation, the perferryl configuration serves to reduce the barrier for the C–H bond activation, since the ground-state adiabatic surface related to the ferryl species tends to get even lower as the avoided crossing interaction increases. Multireference-based methods will be needed for a qualitatively correct treatment of adiabatic surfaces for real states. In intermediate cases, a simple picture of the correlation between the states of reactants and those of intermediates is not possible, since the probability for transition from one adiabatic surface to the other is no longer close to unity nor to zero; the branches of the two avoiding surfaces become essentially a problem of dynamics.

All four TSs, $^2TS1a^*$, 4TS1a , 2TS1a , and $^2TS1a''$, have an almost linear alignment of the oxo group, a transferring hydrogen atom (hereafter denoted by H'), and the center carbon atom of the substrate (C_2) with a C_2 – H' –O angle of 172–176° and a bent H' –O–Fe orientation by 120–126°, as shown in Figure 4, reflecting radical reactivity of π electrons without any tendency for concerted oxygen insertion. Among these, the perferryl species, $^2TS1a^*$, has salient structural features. A short C_2 – H' bond length (1.242 Å) and a long O– H' bond (1.308 Å) mean that $^2TS1a^*$ is located to be

exceptionally early along the reaction coordinate, in accordance with the fact that the activation barrier for the perferryl species is only 2.5 (3.0) with BS1 (BS2) kcal mol⁻¹, with reference to $^22a^*$, which is much smaller than the corresponding values for the ferryl species (10–17 kcal mol⁻¹). Moreover, $^2TS1a^*$ has an alternant spin wave, $Fe\uparrow(1.73)-O\downarrow(-0.22)-H'\uparrow(0.03)-R\downarrow(-0.41)$ (BS2), which should be compared with a “local triplet” situation at the iron–oxo core for the higher-lying ferryl species, 2TS1a , $Fe\uparrow(1.02)-O\uparrow(0.50)-H'\downarrow(-0.04)-R\uparrow(0.54)$. The participation of the perferryl species in the C–H bond activation can also be deduced from the fact that the spin density on the substrate is negative at $^2TS1a^*$ [-0.43 (-0.41) with BS1 (BS2)], as a result of the transfer of an up-spin electron from the substrate to the oxo ligand, in contrast with the positive spin density at 2TS1a [0.56 (0.54)]. We can rationalize these distinct features of $^2TS1a^*$ in terms of the unique electronic properties of the perferryl–oxo species $^21^*$, as already argued,²¹ which has a partially cleaved π -bond and thereby enhance the ability to abstract a hydrogen atom from the inert C–H bond, in such a way that one π electron is effectively localized on a small space of region (the oxo ligand), as depicted in Figure 2. In fact, $^22a^*$ has a stretched Fe–O bond (1.777 Å) and exhibits atomic radical character at the oxo ligand with a negative spin [-0.85 (-0.78) with BS1 (BS2)]. As an additional feature, the Fe–S bond trans to the Fe–O bond is shortened (2.3–2.4 Å) throughout the reaction to activate the oxo ligand and to stabilize $^22a^*$, $^2TS1a^*$, and $^23a^*$.

Figure 5 depicts how the orbital occupancies and bonding patterns of the reactant complexes, $2a$, are transformed into those of the intermediate complexes, $3a$, for several doublet configurations. These diagrams are constructed on the basis of natural orbitals (Figures S3–S6, Supporting Information) and spin density distributions (Tables S2–S4, Supporting Informa-

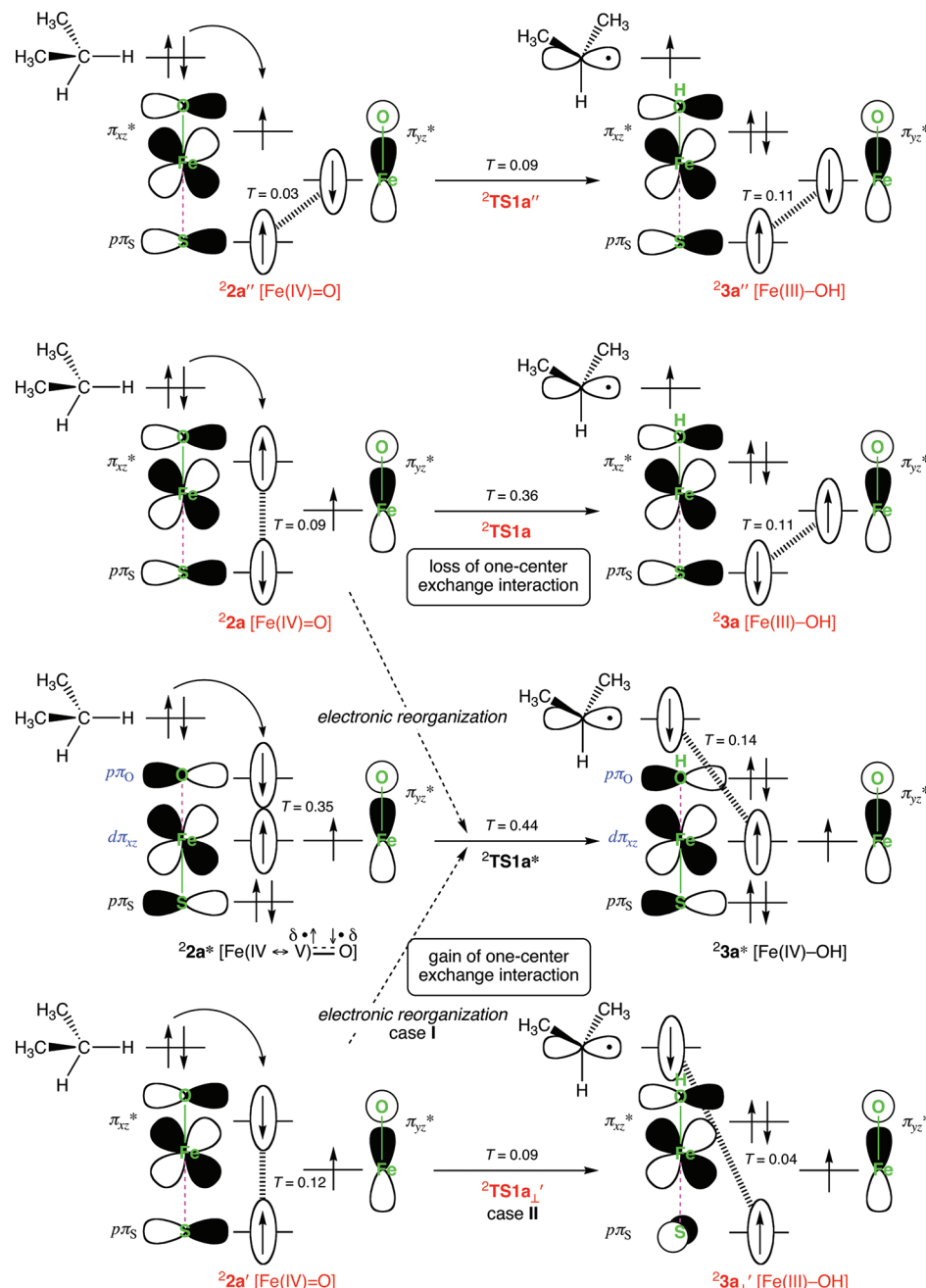


Figure 5. Schematic illustration of how orbital occupancies and bonding patterns of several doublet configurations transform during the secondary hydrogen-atom abstraction from propane by compound I (SCH₃ model, 1); electrons in formally paired spin-polarized orbitals, ψ_{HONO}^{\pm} (eq 2a), are marked by two ellipses with a hashed line representing a bonding interaction between the two spin-paired electrons in ψ_{HONO}^{\pm} .

tion) by focusing on active electrons residing in active orbitals, HONO, LUNO, and SONO. HONO and LUNO are combined to describe a weak bond pair, leading to effectively localized electrons in spin-polarized orbitals marked by two ellipses with a overlap integral T (eq 2a) and there remains a formally noninteracting electron in SONO (eq 2b). It is instructive to compare the ferryl and perferryl species. Figure 6 displays two sets of natural orbitals for the C-H bond activation: one originating from the ferryl-oxo species $^2\text{2a}$ (the left-hand side of Figure 6) and the other from the perferryl-oxo species $^2\text{2a}^*$ (right-hand side). Features of HONO, LUNO, and SONO for weakly interacting precursor complexes, $^2\text{2a}$ and $^2\text{2a}^*$, are essentially the same as those for isolated compound I, $^2\text{1}$ and $^2\text{1}^*$, as previously noted.²¹ Large and small

weights on the S atom for $^2\text{2a}$ and $^2\text{2a}^*$ imply the presence and absence of a radical hole on the thiolate ligand. The amplitude pattern of HONO along the O-Fe-S axis deserves explicit emphasis. The node property of HONO, i.e., the existence or nonexistence of nodal planes cutting through the Fe-O and Fe-S bonds is reversed between $^2\text{2a}$ and $^2\text{2a}^*$. This difference causes the different modes of spin polarization for $^2\text{2a}$ and $^2\text{2a}^*$. In $^2\text{2a}$, $\pi \rightarrow \pi^*$ pseudo double excitation is promoted at the Fe-S bond, leading to a ligand-based radical. In contrast, in $^2\text{2a}^*$, $\pi \rightarrow \pi^*$ excitation is effective at the Fe-O bond, inducing some unpaired spin density appearing on the oxo ligand prior to the reaction of $^2\text{1}^*$ with propane.

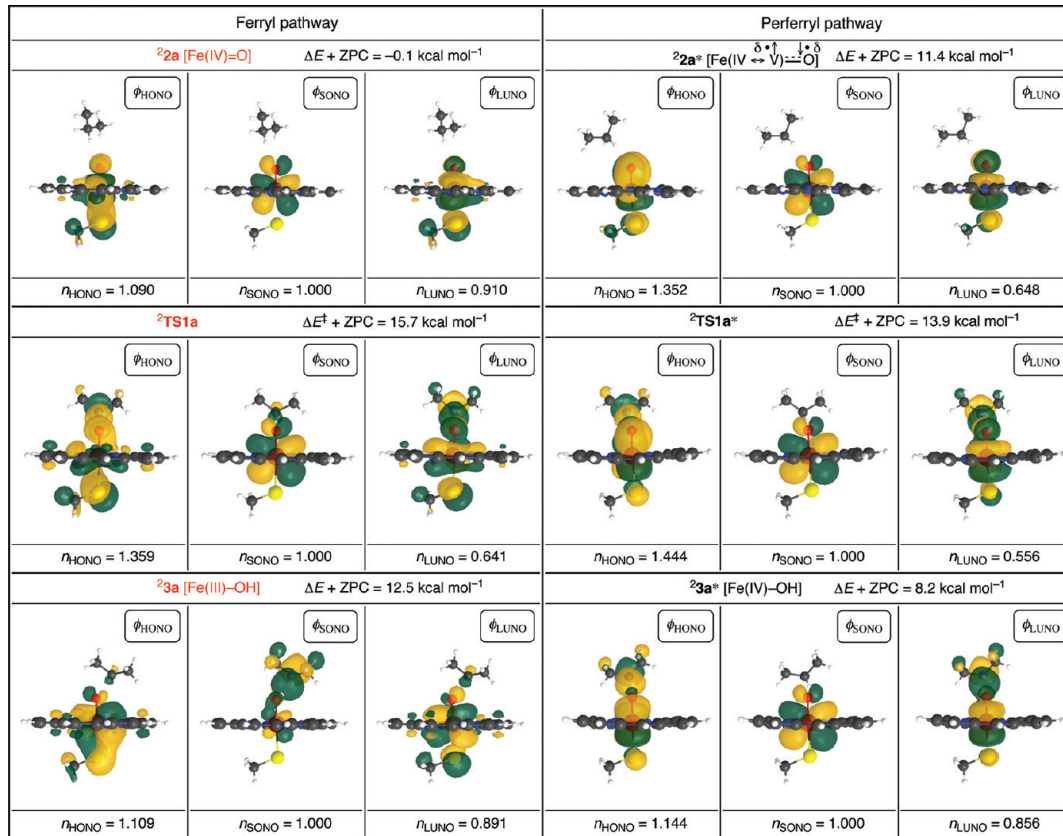


Figure 6. HONO (ϕ_{HONO}), LUNO (ϕ_{LUNO}), and SONO (ϕ_{SONO}) and their occupation numbers (n_{HONO} , n_{LUNO} , and n_{SONO}) for reactant complexes (²2a and ²2a*), transition structures (²TS1a and ²TS1a*), and intermediate complexes (²3a and ²3a*), at the B3LYP/BS1 level.

Transfer of a hydrogen atom from propane to the oxo ligand distorts the natural orbitals in an entirely different manner. For the pathway nascent from the ferryl–oxo species, ²2a \rightarrow ²TS1a \rightarrow ²3a, SONO varies from the π_{yz}^* orbital of the ferryl–oxo core to the $p\sigma_R$ orbital of the isopropyl radical with the simultaneous rotation of HONO and LUNO from the π_{xz}^* orbital of the ferryl–oxo core to the originally SONO π_{yz}^* orbital of the ferric–hydroxo core, each delocalized over the thiolate ligand. This reorganization of bonding pattern, as schematically depicted in the second from the top in Figure 5, is caused by correlations among three electron spins, which is an immediate consequence of the Pauli exclusion principle. When electrons have the same spin, the probability of finding them at the same region of space vanishes by the requirement imposed by permutation symmetry for fermions. In contrast, when electrons have opposite spins, there is enhanced probability of finding them at the same region of space, so that electrons in the HONO and LUNO tend to avoid an electron of opposite spin in SONO for minimizing electron–electron repulsion between the bonding pair and the non-bonding electron.⁴¹ The orbital transformation is not smooth between ²2a and ²3a, and it is also energy demanding due to the loss of one-center exchange interaction at the iron–oxo core. On the other hand, throughout the C–H bond activation by the perferryl–oxo species, ²2a* \rightarrow ²TS1a* \rightarrow ²3a*, SONO remains virtually unaffected as the π_{yz}^* orbital of the iron–oxo core, and HONO and LUNO, which now less spread in the thiolate ligand, are smoothly transformed into the combinations of the $d\pi_{xz}$ atomic orbital of the ferryl ion and the $p\sigma_R$ orbital of the isopropyl radical in ²3a*. This reorganization of bonding pattern, as displayed in the second from the bottom in Figure 5,

naturally realizes an energetically favorable situation, in that formally singlet-paired electrons in the spin-polarized orbitals are disposed in an advantageous manner relative to a third up-spin electron in SONO (the π_{yz}^* orbital) with favorable “local triplet” coupling in two orthogonal orbitals on the same center and unfavorable “local singlet” coupling at a long distance. This ensures a smooth transformation from ²2a* to ²3a* and stabilizes ²3a* by a significant one-center exchange interaction.

The several features of ²3a* are shared with its quartet counterpart, ⁴3a. Both configurations have an identical orbital occupancy, $(\delta_{xy})^2(d\pi_{xz})^\dagger(\pi_{yz}^*)^\dagger(p\sigma_R)^{\dagger(\dagger)}$, which can be verified by significant spin density on the Fe center close to 2.0 (1.7–1.9), residual spin density on the ligands (<0.15), and almost unity spin density on the substrate radical (± 1.0), as well as a relatively short Fe–S bond length (2.3–2.4 Å) for exerting the trans effect. Such similarity also holds for TSs, ⁴TS1a and ²TS1a*. These results imply that electronic relaxation should occur to take a lowest-energy pathway from the pair of the ground configurations of the ferryl–oxo complex $\{^4\text{2a}, ^2\text{2a}\}_G$ to the pair of the ground configurations for the ferryl–hydroxo intermediate $\{^4\text{3a}, ^2\text{3a}^*\}_G$, although the probability of decay may not necessarily be large. This electronic reorganization leading to $\{^4\text{3a}, ^2\text{3a}^*\}_G$ profits greatly from the exchange energy associated with one-center overlap density between two orthogonal $d\pi_{xz}$ and $d\pi_{yz}$ atomic orbitals on the same Fe center. On the other hand, the wave function for ²3a has much in common with that for ²3a'', which arises from the same orbital occupancy, $(\delta_{xy})^2(p\pi_S)^\dagger(\pi_{yz}^*)^\dagger(p\sigma_R)^\dagger$. The degenerate pair of the ferric–hydroxo species $\{^2\text{3a}, ^2\text{3a}''\}_E$ is prohibited from electronic reorganization due to substantial one-center electron repulsion between electrons with antiparallel spins. For this

reason, $\{^2\text{3a}, ^2\text{3a}''\}_E$ lies about 4 kcal mol⁻¹ above $\{^4\text{3a}, ^2\text{3a}^*\}_G$, as shown in Figure 3B.

3.2.2. SCH_3 Model: Case II. The π -bonding interaction between the ferryl–oxo core and the thiolate ligand for the SCH_3 model of ferryl compound I, $^{2,4}\text{1}$, is estimated to be very weak ($T < 0.1$), indicating that the rotational barrier about the Fe–S bond should be low. One might expect that the conformational change of the SCH_3 ligand relative to the $\text{C}_2\text{O}\text{—Fe}$ plane should affect the effective overlap between the $d\pi_{xz}$ and $p\pi_S$ orbitals and hence have chemical consequences. Present B3LYP calculations have found this expectation to be the case, as far as the SCH_3 model is concerned. Rotation about the Fe–S bond by about 30–60° takes $^4\text{TS1a}$, $^2\text{TS1a}$, $^2\text{TS1a}^*$, and $^2\text{TS1a}''$ configurations into new stationary points with only one imaginary frequency corresponding to the transfer of a hydrogen atom, denoted as $^4\text{TS1a}_{\perp}$, $^2\text{TS1a}_{\perp}$, $^2\text{TS1a}_{\perp}'$, and $^2\text{TS1a}_{\perp}''$. Inspection of natural orbitals (Figure S5, Supporting Information) shows that all the newly found TSs, $^4\text{TS1a}_{\perp}$, $^2\text{TS1a}_{\perp}$, $^2\text{TS1a}_{\perp}'$, except for $^2\text{TS1a}_{\perp}''$,³⁸ have HONO and LUNO that bear an appreciable weight on the $p\pi_S$ orbital spanning in the nodal plane of the π_{xz}^* orbital of the ferryl–oxo core, which we classify into case II. The SCH_3 ligand, at which an unpaired electron is localized, is rotated out of the plane containing the π_{xz}^* orbital so that the unpaired electron becomes largely confined to the SCH_3 ligand, as illustrated in the bottom in Figure 5. Two TSs, $^4\text{TS1a}_{\perp}$ and $^2\text{TS1a}_{\perp}'$, in particular differ distinctly from $^4\text{TS1a}$ and $^2\text{TS1a}^*$, in that the former two TSs are free from electronic reorganization, which is also reflected in the geometrical features that $^4\text{TS1a}_{\perp}$ and $^2\text{TS1a}_{\perp}'$ have a relatively long Fe–S bond distance ($r_{\text{FeS}} = 2.6$ Å), as compared with those of $^4\text{TS1a}$ and $^2\text{TS1a}^*$ (2.394 Å) and that $^2\text{TS1a}_{\perp}'$ is no longer an early TS, as shown in Figure 4. For this reason, $^4\text{TS1a}_{\perp}$ and $^2\text{TS1a}_{\perp}'$ are placed above $^4\text{TS1a}$ and $^2\text{TS1a}^*$ by 2.3 and 5.4 kcal mol⁻¹ with BS1, although $^2\text{TS1a}_{\perp}$ and $^2\text{TS1a}_{\perp}''$ lie at almost the same energy level as $^2\text{TS1a}$ and $^2\text{TS1a}''$ with differences of only 1.0 and 0.6 kcal mol⁻¹, as shown in Figure 3. Spin density distributions further confirm that $^4\text{TS1a}_{\perp}$ and $^2\text{TS1a}_{\perp}'$ are not involved in electronic reorganization; spin populations are less than 1.00 on the Fe atom [0.88 (0.96) for $^4\text{TS1a}_{\perp}$ and 0.89 (0.81) for $^2\text{TS1a}_{\perp}'$ with BS1 (BS2)] and close to 1.00 on the ligands [0.97 (0.93) and 0.97 (0.99)], while, for $^4\text{TS1a}$ and $^2\text{TS1a}^*$, they are more than 1.00 on the Fe atom [1.30 (1.22) for $^4\text{TS1a}$ and 1.91 (1.73) for $^2\text{TS1a}^*$] and not significant on the ligands [0.51 (0.61) and –0.25 (–0.14)]. $^4\text{TS1a}_{\perp}$ and $^2\text{TS1a}_{\perp}'$ and their associated ferric–hydroxo intermediates, $^4\text{3a}_{\perp}$ and $^2\text{3a}_{\perp}'$, are, therefore, not isoelectronic to $^4\text{TS1a}$ and $^2\text{TS1a}^*$ and ferryl–hydroxo intermediates, $^4\text{3a}$ and $^2\text{3a}^*$. $^4\text{TS1a}_{\perp}$ and $^2\text{TS1a}_{\perp}'$ could be located only in case II, since suitably oriented $d\pi_{xz}$ and $p\pi_S$ orbitals on the Fe and S atoms for π bonding (case I) permit electronic reorganization to occur and automatically lead to the lower-lying $^4\text{TS1a}$ and $^2\text{TS1a}^*$. In contrast, $^2\text{TS1a}_{\perp}$ and $^2\text{TS1a}_{\perp}''$ are nothing more than bond-rotated isomers of $^2\text{TS1a}$ and $^2\text{TS1a}''$; bond-rotated isomers $^2\text{TS1a}$ and $^2\text{TS1a}_{\perp}$ ($^2\text{TS1a}''$ and $^2\text{TS1a}_{\perp}''$) both have common electronic characteristics and connect to a ferric–hydroxo intermediate, $^2\text{3a}$ ($^2\text{3a}''$), irrespective of the ligand orientation. A rotation about the Fe–S bond of $^2\text{TS1a}$ ($^2\text{TS1a}''$) only interchanges two bond-rotated isomers that are on the potential surface of a single electronic configuration, with a small perturbation on its stability to within 1 kcal mol⁻¹.

In case II, the energy gap between the ground and excited configurations gradually shrinks, as the hydrogen-abstraction reaction progresses, leading to the 4-fold nearly degenerate configurations of the radical intermediate complex to less than 0.3 kcal mol⁻¹, as shown in Figure 3A, even though they have ununiform spin distributions: $\{^4\text{2a}, ^2\text{2a}\}_G$, $\{^2\text{2a}', ^2\text{2a}''\}_E \rightarrow \{^4\text{3a}_{\perp}, ^2\text{3a}, ^2\text{3a}_{\perp}', ^2\text{3a}''\}_E$. Such an isoenergetic manifold of the excited configurations for 3a cannot be resolved even after the AP correction is applied in a similar manner as described in section 3.1, leading to 3-fold nearly degenerate states (two independent doublets and one quartet; the spin-projected states of 3a are not shown in Figure 3 for clarity). The reason for the energetic proximity of the configurations (or states) of the radical intermediate complex 3a is that, since individual spins are localized into spatially separated regions, there is little difference in electron repulsion between them. This is in sharp contrast with the situation in the reactant complex 2a .

3.2.3. SH Model. Similarly to the case of the SCH_3 model, we have also examined the reaction of the SH-ligated compound I, denoted by 1_{SH} , with propane. Energy profiles are shown in Figure S1B (Supporting Information), and key geometrical features and spin and charge distributions for reactant complexes (2a_{SH}), TSs (TS1a_{SH}), and intermediate complexes (3a_{SH}) are given in Figure S7 and Tables S5–S7 (Supporting Information). We can see from these results that the overall picture is similar as in case I for the SCH_3 model; there are at least four configurations, $^2\text{TS1a}_{\text{SH}}^*$, $^4\text{TS1a}_{\text{SH}}$, $^2\text{TS1a}_{\text{SH}}$, and $^2\text{TS1a}_{\text{SH}}''$, in the region of transition state, of which $^2\text{TS1a}_{\text{SH}}^*$ lies the lowest. The computed activation barriers relative to the quartet reactant complex $^4\text{2a}_{\text{SH}}$ (11.7–19.4 kcal mol⁻¹) are comparable to the values reported previously (13.9–15.8 kcal mol⁻¹ relative to separated reactants).⁴² The lowest-lying $^2\text{TS1a}_{\text{SH}}^*$ is found to be nascent from the perferryl–oxo precursor complex, $^2\text{2a}_{\text{SH}}^*$, not the ferryl one, according to a IRC path. In fact, $^2\text{2a}_{\text{SH}}^*$ and $^2\text{TS1a}_{\text{SH}}^*$ both possess salient features inherent in the perferryl species, as highlighted above for the SCH_3 model, which include a long Fe–O bond length for preactivation of $^2\text{2a}_{\text{SH}}^*$ (1.784 Å), short Fe–S bond lengths of $^2\text{2a}_{\text{SH}}^*$ and $^2\text{TS1a}_{\text{SH}}^*$ (2.35–2.37 Å) for exerting the trans effect, early reactant-like nature of $^2\text{TS1a}_{\text{SH}}^*$ [a short $\text{C}_2\text{H}'$ bond length (1.245 Å) and a long O–H' bond length (1.307 Å)], substantial spin population (close to 2.0) on the Fe center of $^2\text{2a}_{\text{SH}}^*$ and $^2\text{TS1a}_{\text{SH}}^*$ [1.90 (1.77) and 1.89 (1.76) with BS1 (BS2)], negative spin density on the oxo ligand of $^2\text{2a}_{\text{SH}}^*$ [–0.85 (–0.78) with BS1 (BS2)], alternating spin signs of $^2\text{TS1a}_{\text{SH}}^*$ [$\text{Fe}\uparrow(1.76)\text{—O}\downarrow(-0.20)\text{—H}'\uparrow(0.02)\text{—R}\downarrow(-0.41)$ (BS2)], and so on. The perferryl–oxo oxidant in $^2\text{2a}_{\text{SH}}^*$ containing a highly reactive oxygen atom can abstract a hydrogen atom from propane with a substantially lower barrier [2.2 (0.6) kcal mol⁻¹ with BS1 (BS2)] than the ferryl–oxo oxidant in $^{2,4}\text{2a}_{\text{SH}}$ [13.2–14.8 (13.4–17.6) kcal mol⁻¹].

3.2.4. Bulk Polarity Effect. Energy profiles in a polarizing medium ($\epsilon = 4.0$), which include electronic energies, zero-point vibrational energies, entropies, and solvation energies, are indicated in Figure S1C,D (Supporting Information) for both the SCH_3 and SH models. Apart from the entropic effect ($-T\Delta S$) required to achieve a more ordered TS geometry from a loosely bound reactant complex, which consistently raises the activation barrier by about 6 kcal mol⁻¹, qualitative features are similar as in the gas-phase case (Figure S1A,B, Supporting Information). Comparison between the SCH_3 and SH models indicates that the activation energies in the gas phase are lower by about 2–3 kcal mol⁻¹ in the SH model than in the SCH_3

Table 2. Relative Energies of Transition Structures ($TS1b_{SH}$) for the Hydrogen-Atom Abstraction from Methane by Compound I (SH Model, 1_{SH}) at the Various Levels of Theory^a

	B3LYP/BS1//BS1	B3LYP/BS2//BS2	CAM-B3LYP/BS2//BS2	HSE06/BS2//BS2	M06/BS2//BS2	ω B97X-D/BS2//BS2
$^4TS1b_{SH}$	20.0	19.7	20.8	15.6	16.5	18.9
$^2TS1b_{SH}$	21.8 (21.9) ^b	21.9 (22.1) ^b	19.5 (19.6) ^b	18.8 (19.0) ^b	20.0 (20.5) ^b	18.0 (18.0) ^b
$^2TS1b_{SH}^*$	17.7 (6.3) ^c	17.6 (7.2) ^c	18.9 (7.5) ^c	13.0 (5.7) ^c	13.2 (6.7) ^c	17.5 (5.8) ^c

^aRelative energies including ZPC with respect to the $^42b_{SH}$ configuration are given in kcal mol⁻¹. ^bRelative to the $^22b_{SH}$ configuration. ^cRelative to the $^22b_{SH}^*$ configuration.

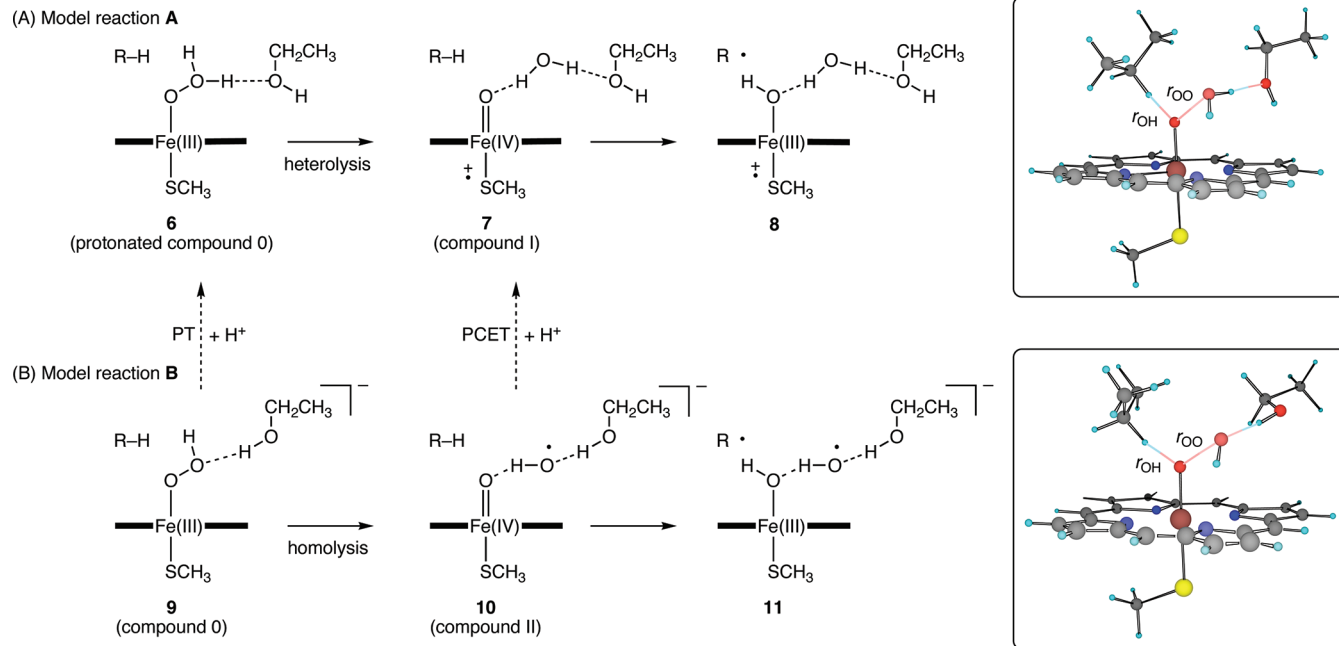


Figure 7. Two model reactions for O–O and C–H bond activation; two parameters (r_{OO} and r_{OH}), as indicated in rectangular frames, are used to explore potential surfaces; dashed arrows indicate proton transfer (PT) and proton-coupled electron transfer (PCET).

model, except for $^2TS1a_{SH}$, while the activation free energies in the polarizing medium are practically identical for both the SCH_3 and SH models, differing only by <1.7 kcal mol⁻¹.

3.2.5. Effects of Basis Sets and Functionals. To check the stability of the B3LYP/BS1 results, the relative energies of the three TSs, $^2TS1b_{SH}^*$, $^4TS1b_{SH}$, and $^2TS1b_{SH}$, have been studied for the hydrogen abstraction from the simplest alkane, methane (**b**), by the HS model of compound I, 1_{SH} , by full optimizations using five functionals of various types (B3LYP, CAM-B3LYP, HSE06, M06, and ω B97X-D), combined with the large all-electron basis set BS2. Table 2 compares the energetics of the TSs at different levels of theory; more details including energy diagrams, geometrical parameters, and charge and spin populations are given in Figure S11 and Tables S8 and S9 (Supporting Information). As expected from the larger C–H bond dissociation energy of methane (100.0 kcal mol⁻¹) than that of propane (92.2 kcal mol⁻¹), the B3LYP/BS1 method gives larger barriers (relative to $^42b_{SH}$) for hydrogen abstraction from methane than those for propane by about 6–7 kcal mol⁻¹; however, the energy ordering is predicted to be the same between the substrates, $^2TS1b_{SH}^* < ^4TS1b_{SH} < ^2TS1b_{SH}$. Changing the basis set from small BS1 to large BS2 has a small effect on the energetics with deviations being below 1 kcal mol⁻¹. The long-range correction through CAM selectively stabilizes the ferryl TS, $^2TS1b_{SH}$, by 2.4 kcal mol⁻¹ and destabilizes the perferryl TSs, $^2TS1b_{SH}^*$ and $^4TS1b_{SH}$, by 1.1–1.3 kcal mol⁻¹, leading to closely lying TSs within a range of 1.9

kcal mol⁻¹. The relative energies of the three TSs follow the order $^2TS1b_{SH}^* < ^2TS1b_{SH} < ^4TS1b_{SH}$, with the stabilities of $^4TS1b_{SH}$ and $^2TS1b_{SH}$ inverted. The same trend is observed in the results of another long-range corrected functional, ω B97X-D. In such a case, it is really necessary that several configurations be superposed. In contrast, the screened functional, HSE06, stabilizes the perferryl TSs, $^2TS1b_{SH}^*$ and $^4TS1b_{SH}$, more than the ferryl TS, $^2TS1b_{SH}$, giving rise to a relatively large $^2TS1b_{SH}^*/^2TS1b_{SH}$ energy separation of 5.8 kcal mol⁻¹. The HSE06 results are rather similar to those of the hybrid meta-GGA, M06, which prefers $^2TS1b_{SH}^*$ to $^2TS1b_{SH}$ by 6.8 kcal mol⁻¹.

Even though the variation in energetics is obtained with various functionals, one important point becomes very clear, which is quite stable with respect to the basis set and functional; like the case with propane, barriers for the reaction of $^21_{SH}^*$ with methane (5.7–7.5 kcal mol⁻¹) are substantially lower than those for $^41_{SH}$ (15.6–22.1 kcal mol⁻¹), as shown in parentheses in Table 2. It is obvious from these results that the perferryl–oxo oxidant is much more reactive than the ferryl–oxo oxidant by several orders of magnitude in rate constant. The presence of a highly reactive perferryl–oxo species at a relatively low energy level led us to consider further the possibility for multiple pathways for P450-catalyzed hydroxylation that involves two active oxidants (ferryl and perferryl compound I). This subject will be addressed in the next section.

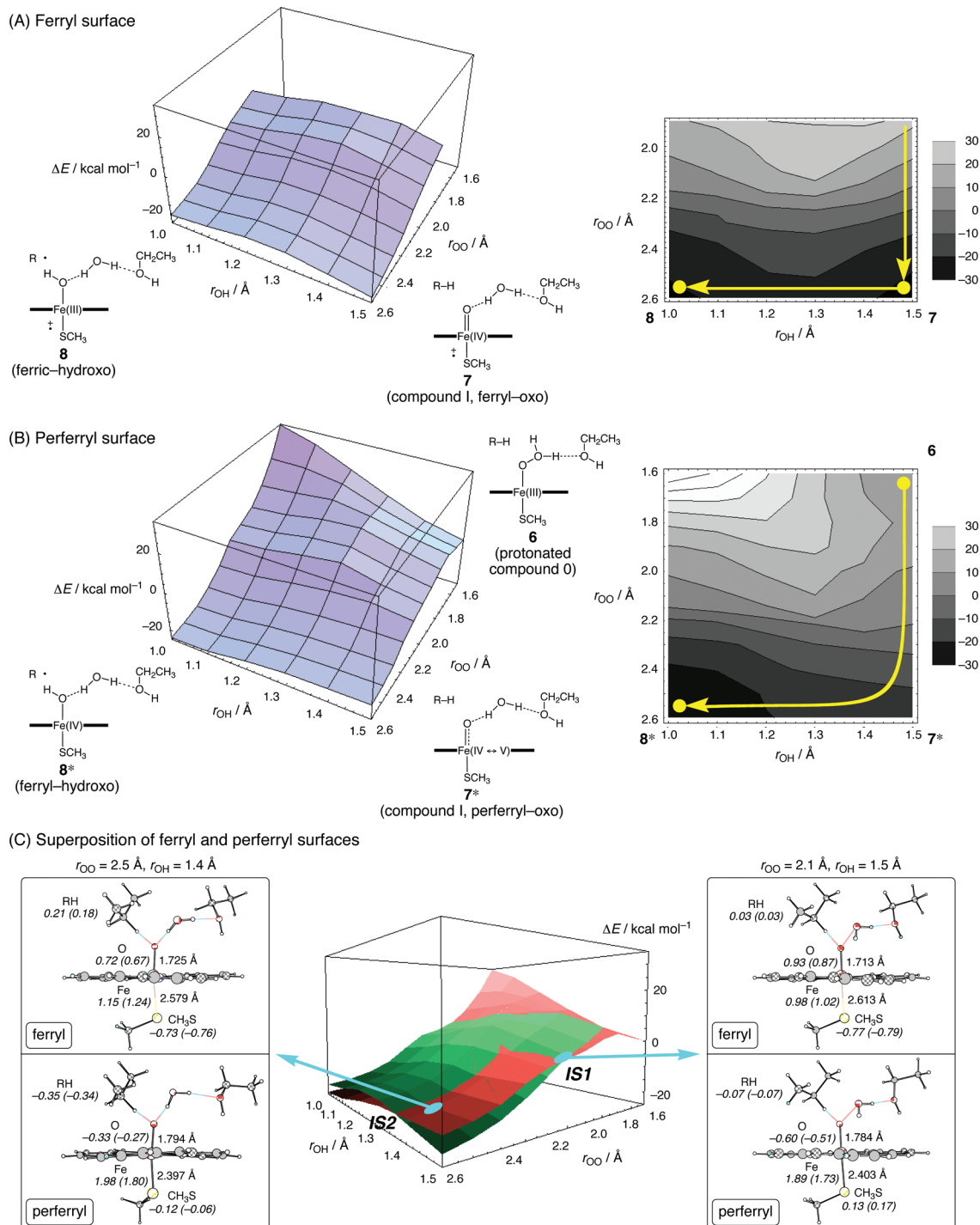
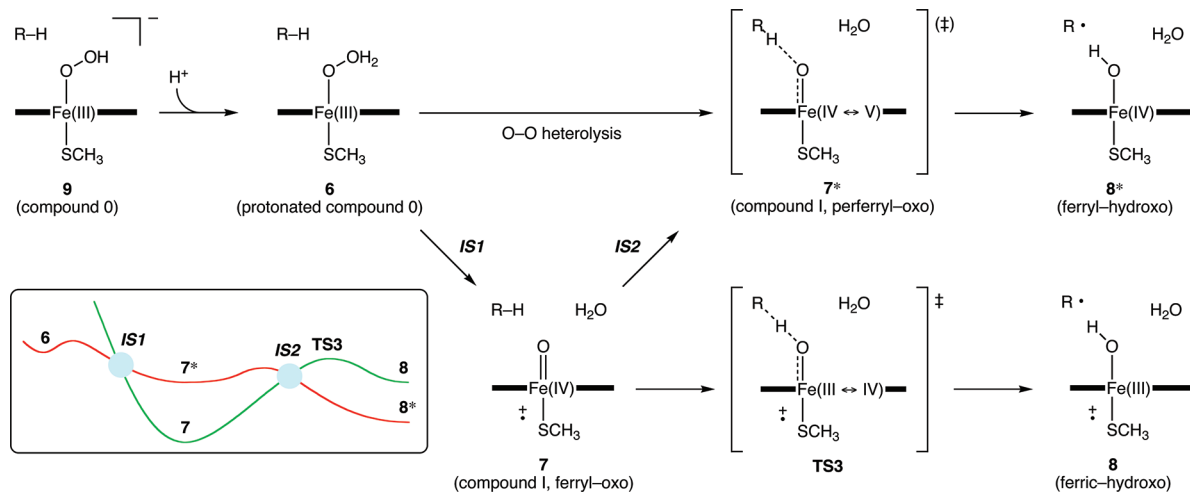


Figure 8. Three-dimensional plots and counter lines of ferryl (A) and perferryl (B) doublet surfaces in the (r_{OO} , r_{OH}) subspace and the superposition of the two surfaces (C) for the model reaction A at the B3LYP/BS1 level; ferryl and perferryl surfaces are shown in green and red; protonated compound 0 (6) is used as a reference; Mulliken spin populations with BS1 (BS2) are given in italics.

3.3. Role of Perferryl-Oxo Oxidant in O–O and C–H Bond Activation. The binding of O_2 to the vacant coordination position of the pentacoordinate ferrous [Fe(II)] complex followed by further two-electron reduction and protonation leads to the formation of compound 0 [$\text{Fe(III)}-\text{OOH}^-$] (Chart 1), which is experimentally observed as the last intermediate in the catalytic cycle of P450.^{3b,43} The conversion of compound 0 to compound I is generally assumed to be initiated by the protonation of the distal (outer) oxygen of compound 0 followed by the heterolysis of the resulting $\text{FeO}-$

OH_2 bond, which might come from the presence of the “push” effect by the proximal thiolate ligation and a conserved acid–alcohol side-chain pair in the distal pocket that can function as a proton transport pathway required to protonate the distal OH moiety of compound 0.⁴⁴ Dey et al. found that the thiolate ligand enhances the proton affinity of compound 0, rather than weakens the $\text{FeO}-\text{OH}$ bond, thereby facilitating the proton-induced heterolysis of the $\text{FeO}-\text{OH}_2$ bond.⁴⁵ Early QM and QM/MM calculations indicated that the protonated compound 0 [$\text{Fe(III)}-\text{OOH}_2$] is not an intermediate but rather a

Scheme 2



transition state for the proton-assisted formation of compound I,⁴⁶ while recent QM/MM studies suggested that it may be a genuine intermediate,⁴⁷ which is, however, very high in energy, as compared with compound 0.^{47b} In contrast, Bach and Dmitrenko proposed an alternative mechanism, in which the FeO–OH bond cleavage in compound 0 occurs in a homolytic fashion, leading to a complex of compound II and a hydroxyl radical (HO•), which is stabilized by the increasing basicity of the ferryl oxygen in the presence of the thiolate ligand.⁴⁸ In their “somersault” rearrangement mechanism, this hydrogen-bonded “inverted” HO• is supposed to act as an oxidant for alkane hydroxylation.⁴⁸ On the other hand, Zheng et al. postulated a hybrid homolytic–heterolytic mechanism,^{47b} in which the initial homolytic O–O bond breaking is immediately followed by a subsequent proton-coupled electron transfer to give compound I and a water molecule.

We consider herein two model reactions, A and B, as shown in Figure 7, to investigate the role of the perferryl species in the O–O bond activation starting from compound 0 and in the subsequent C–H bond activation. The first model reaction A starts with a weakly bound complex of propane and protonated compound 0 that is hydrogen-bonded to ethanol, a model of highly conserved threonine, 6, and ends up with a ferric–hydroxo (or ferryl–hydroxo, not shown in Figure 7) species that is encountered with a isopropyl radical and hydrogen-bonded to ethanol via a water molecule, 8 (or 8*) (Figure 7A). This reaction is investigated with the aim of understanding the behaviors of the ferryl and perferryl species during the heterolytic FeO–OH₂ bond cleavage. In this reaction, the ferryl (or perferryl) compound I in 7 (or 7*) acts as an oxidant. The homolysis of the FeO–OH bond is modeled by the second reaction B, in which a weakly bound complex of propane, compound 0, and ethanol, 9, is converted into a complex of isopropyl radical, ferric–hydroxo species, hydroxyl radical, and ethanol, 11 (Figure 7B). Although there are two oxidants, compound II and bound hydroxyl radical, capable of abstracting a hydrogen atom from propane in an intermediate complex, 10, we have investigated only the reactivity of compound II. The total charge of the system is neutral in reaction A and –1 in reaction B. We focus herein on the results of the doublet state, which is the ground species of compound 0.^{12,46a} Two parameters are used to explore potential surfaces, as shown in rectangular frames in Figure 7: one is the distance

between the two oxygen atoms of the dissociating peroxide bond (r_{OO}) and the other is the distance between the proximal (inner) oxygen and the migrating hydrogen atom (r_{OH}). Since the substrate is tightly held in close proximity to the heme moiety, which can be achieved by the hydrogen bonding between the carbonyl group of camphor and Tyr96 in the case of the enzyme P450cam,⁴⁹ the bond length between the Fe-coordinated oxygen and the center carbon of propane is also kept fixed at 2.6 Å, which is close to those for hydrogen-abstraction TSs. We have explored 11×6 grids of potential surfaces with r_{OO} varying from 1.6 to 2.6 Å with 0.1 Å interval and r_{OH} from 1.0 to 1.5 Å with 0.1 Å interval for the model reactions A and B; each grid point is obtained at the B3LYP/BS1 level by freezing the two parameters (r_{OO} and r_{OH}) at a given set of values and optimizing all other degrees of freedom except for the bond length between the Fe-coordinated oxygen and the center carbon of propane. All relative energies reported in this section do not include ZPC.

Figure 8 depicts the three-dimensional plots and counter lines of the grids of ferryl (A) and perferryl (B) doublet surfaces in the (r_{OO} , r_{OH}) subspace and their superposition (C) for the model reaction A. The ferryl surface shows two appreciable potential wells, which correspond to compound I, 7, and radical intermediate complex, 8 (Figure 8A). Calculations show no stability of the ferrous configuration of protonated compound 0; efforts to obtain this species at short O–O bond distances ($r_{OO} < 1.9$ Å) were unsuccessful, and the surface descends monotonically toward the ferryl compound I 7. The ferric–hydroxo intermediate 8 is separated from 7 by a barrier of about 5.6 (7.0) kcal mol^{−1} with BS1 (BS2) for the transfer of a hydrogen atom from propane to the oxo ligand. These results mean that the C–H bond activation by the ferryl–oxo oxidant should occur in a stepwise manner, as shown by two yellow arrows in Figure 8A, which involves an automatic heterolytic FeO–OH₂ bond dissociation to form compound I and a subsequent hydrogen abstraction from propane by the resulting compound I. In the perferryl surface (Figure 8B), there are also two wells, but one of which corresponds to the ferric configuration of protonated compound 0, 6, while the other concerns the ferryl–hydroxo intermediate, 8*. The heterolysis of the FeO–OH₂ bond requires a low barrier of about 3.9 (3.3) kcal mol^{−1} with BS1 (BS2), in agreement with earlier QM/MM studies (SH model, less than 5 kcal mol^{−1}).^{47b} There is a

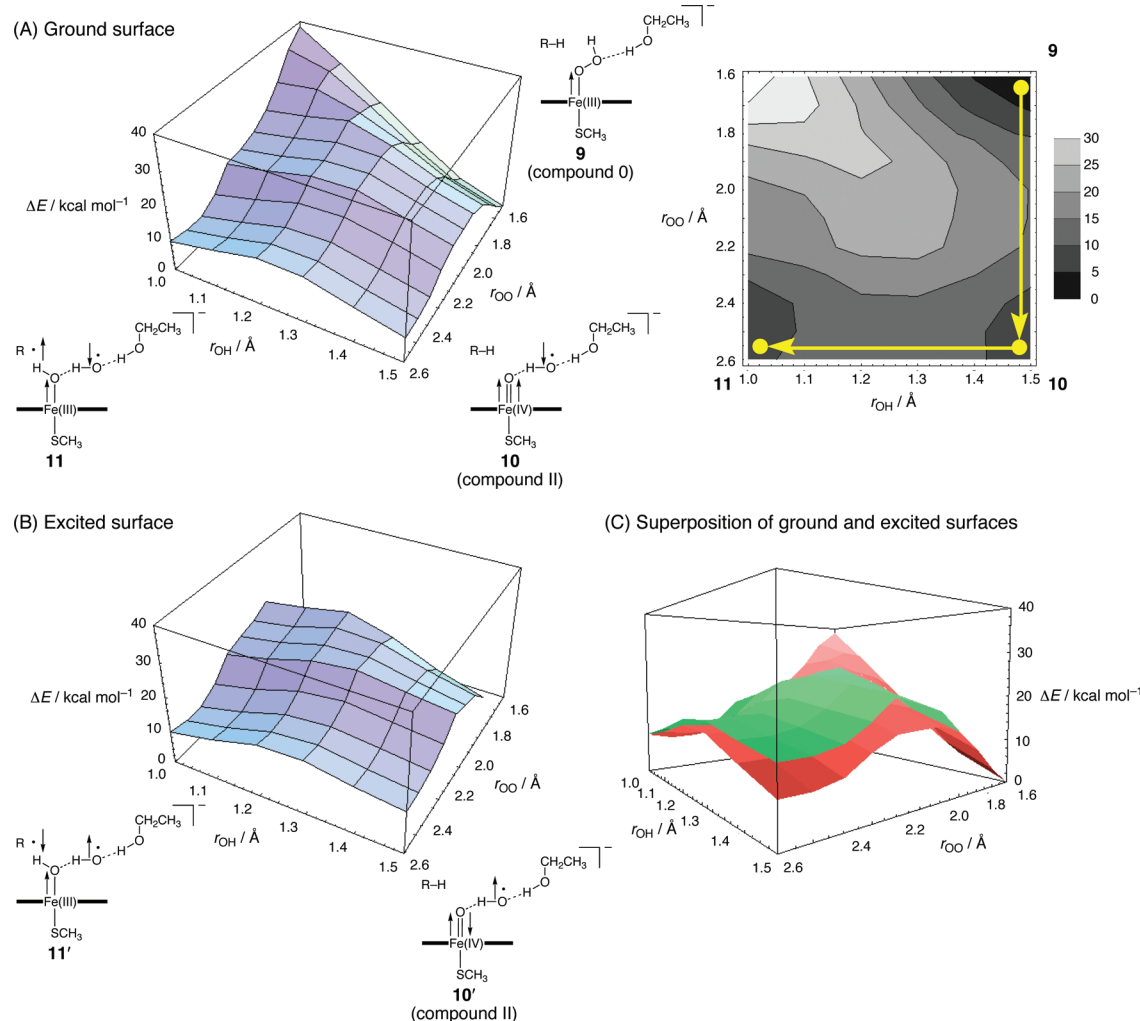


Figure 9. Three-dimensional plots and counter lines of ground (A) and excited (B) doublet surfaces in the (r_{OO} , r_{OH}) subspace and the superposition of the two surfaces (C) for the model reaction B at the B3LYP/BS1 level; ground and excited surfaces are shown in red and green; compound 0 (9) is used as a reference.

reorientation of the hydrogen-bond network at around $r_{\text{OO}} = 2.1 \text{\AA}$, so that the liberated water molecule becomes a hydrogen-bond donor to the oxo ligand. The perferryl–oxo species, 7^* , lies on a flat region of the surface without a significant minimum. It is also important to recall that the BS energy of 7^* is an upper bound to that of the spin-adapted mixed-valent state. Once the tiny barrier for the heterolytic splitting has been overcome, the reaction trajectory will progress downward with successive O–O and C–H bond breaking and O–H bond formation through a shoulder region for 7^* , as shown by one yellow arrow in Figure 8B, producing directly the radical intermediate 8^* with an exothermicity of 24.3 (34.2) kcal mol^{-1} with BS1 (BS2). The diagonal path involving completely simultaneous O–O and C–H bond breaking is prevented by the presence of a ridge. The reason that a small barrier of about 2.5 kcal mol^{-1} for the hydrogen abstraction from the mobile substrate by 21^* , as shown in Figure 3, almost vanishes in the model reaction A can be attributed to the close proximity of the highly reactive oxo ligand to the substrate, which is prerequisite for function, and the presence of a water molecule near the oxo ligand that is released by the heterolytic splitting. Recent QM/MM theoretical studies already pointed out the catalytic role of

the water molecule;⁵⁰ our additional calculations indeed indicate that the electrostatic interaction between the oxo group with developing negative charge and the nearby water molecule lowers the barrier height for the reaction of 1 with propane by about 0.6–2.6 kcal mol^{-1} with ZPC, regardless of the spin state (Figure S12A, Supporting Information).

Scheme 2 summarizes the stepwise and nonsynchronous concerted pathways involving the ferryl–oxo and perferryl–oxo oxidants for the model reaction A (ethanol is omitted for clarity), which can be deduced from the superposition of the two grids, as demonstrated in Figure 8C. Several possibilities arise from the fact that, although the lowest configuration is the perferryl one at the start and end of the reaction, 6 and 8^* , there is a region in which the ferryl configuration is lowest, as schematically illustrated in a rectangular box in Scheme 2. The ferryl species has its energy minimum at the equilibrium geometry of compound I, 7, which is consistently below the perferryl surface [by about 4.5 (5.8) kcal mol^{-1} with BS1 (BS2) at $r_{\text{OO}} = 2.6 \text{\AA}$ and $r_{\text{OH}} = 1.5 \text{\AA}$]. There should be crossover of the energy of the perferryl surface with that of the ferryl surface twice along the reaction trajectory. The apparent crossing seam between the ferryl and perferryl surfaces in the three-dimensional space, as indicated in Figure 8C, is actually not a

real crossing seam in the multidimensional coordinate space. In fact, optimized geometries near the apparent seam, as indicated in rectangular frames in Figure 8C, are not identical on the ferryl and perferryl surfaces; the Fe–S bond length in particular differs by about 0.2 Å. This means that the avoided-crossing region is characterized by abrupt elongation or shrinkage of the Fe–S bond, depending on the mode of spin polarization. This phenomenon is caused by the fact that two alternative bond descriptions for the O–Fe–S unit in compound I have opposite energetic behaviors under an asymmetric stretching mode.²¹ If the electronic transition from the perferryl to ferryl surface happens in the first intersection region during the O–O heterolysis, which lies between $r_{OO} = 2.1$ and 2.2 Å in three dimensions (**IS1** in Figure 8C), the reaction will proceed in a stepwise manner via the ferryl compound I **7** with concomitant energy stabilization. This stepwise process mediated by the redox-active porphyrin/thiolate ligands may be similar to the one proposed for chloroperoxidase catalysis.⁵¹ The second TS for hydrogen abstraction involves either the perferryl (**7***) or ferryl (**TS3**) configuration, depending on whether the electronic reorganization occurs or not when the system goes through the second intersection region, which lies between $r_{OH} = 1.3$ and 1.4 Å in three dimensions (**IS2** in Figure 8C). The fact that the system should undergo abrupt Fe–S bond stretching after the electron shift makes the stepwise pathways quite unfavorable. On the other hand, if the reacting system remains on the diabatic surface during the heterolytic bond cleavage, the reaction will occur on the higher-lying surface for the perferryl compound I, **7***, which will slope downward to the ferryl intermediate, **8***, or may exhibit a small barrier less than about 2.5 kcal mol⁻¹, which is the extreme case for allowing the substrate to move freely in the gas phase (Figure 3). The lifetime of the perferryl compound I will be extremely short, if any. This diabatic surface connects smoothly the lowest configuration of protonated compound 0, **6**, with the lowest configuration of radical intermediate, **8***, without any abrupt electronic and geometric changes at **IS1** and **IS2**, which is very suitable for fast oxidation and serves to save energetic cost. A significant role in making the overall reaction more efficient is played by the appreciably basic thiolate ligand, which can act as the Lewis acid toward the Fe center to engage in facile O–O and C–H bond activation processes.

We now turn to the model reaction **B** indicated in Figure 7. Figure 9 shows three-dimensional plots and counter lines of the grids of the ground (A) and excited (B) doublet surfaces in the (r_{OO} , r_{OH}) subspace and their superposition (C) for the model reaction **B**. Compound 0 has a doublet ground state with a singly occupied π_{xz}^* orbital.^{12,46a} The initial stage of this reaction is characterized by the homolytic dissociation of the FeO–OH bond in compound 0, **9**. There are two spin structures with respect to the dissociating O–O bond, $\uparrow\text{FeO}\uparrow\dots\downarrow\text{OH}$ and $\uparrow\text{FeO}\downarrow\dots\uparrow\text{OH}$, which are usually combined to form singlet and triplet electron pairs. We can predict with fair certainty that, as the FeO–OH bond stretches, the ground state will become better described by the former structure than the latter and vice versa in the excited state, since two unpaired electrons in the FeO moiety are in orthogonal planes (π_{xz}^* and π_{yz}^*) and there is substantial overlap between the π_{xz}^* and π_{yz}^* orbitals. In fact, broken-symmetry (BS) DFT calculations indicate that, after the O–O bond distance exceeds a certain threshold ($r_{OO} > 1.9$ Å), the doublet ground state splits into two BS solutions characterized by the “local triplet” and “local singlet” situations at the ferryl–oxo core, of which the former is

placed well below the latter, as shown in Figure 9C. For the ground configuration of compound II, only the “local triplet” situation is possible. We can exclude the reaction on the quasi-classical “local singlet” surface because of no surface crossing and even more so on the spin-adapted surface for the local singlet state. The ground surface shows three appreciable wells corresponding to compound 0, **9**, compound II, **10**, and radical intermediate complex, **11**, as indicated in Figure 9A. The barrier required for the O–O homolysis in reaction **B** is significant [ca. 14.9 (17.7) kcal mol⁻¹ with BS1 (BS2)], as compared with a low barrier for the O–O heterolysis in reaction **A** [ca. 3.9 (3.3) kcal mol⁻¹]. These estimates are similar to the values obtained by the QM/MM study (SH model, 13–17 kcal mol⁻¹).^{47b} The barrier for the hydrogen-atom abstraction from propane by the resulting compound II (reaction **B**) is also higher than that by compound I (reaction **A**), though not to a significant extent (by about 1 kcal mol⁻¹). The sluggish reactivity of compound II and its model compounds has been reported experimentally⁵² and theoretically.^{50c}

The reacting system **B** is linked to the system **A** by acquiring a proton from the environment either before or after the O–O bond cleavage in compound 0, as indicated by two dashed arrows in Figure 7. The timing of proton transfer or proton-coupled electron transfer in the model reaction **B**, i.e., whether it will occur in **9** or in **10**, will be important to understand the reaction mechanism, since the O–O bond cleavage causes a reverse in the ordering of the ferryl and perferryl surfaces in the model reaction **A**, as shown in Figure 8C. Proton transfer in the early phase of the O–O bond dissociation in compound 0 (**9** → **6**) will give exclusively protonated compound 0 on the perferryl surface, which lies much below the ferryl surface. This event will be immediately followed by proton assisted O–O heterolysis and may preclude the formation of the ferryl compound I, provided that the system remains on the diabatic surface and crosses at **IS1**. On the other hand, compound I generated by a proton-coupled redox event in the late phase of the O–O homolysis (**10** → **7**), i.e., after the TS for the homolytic bond cleavage is passed, will have a propensity to adopt as a ground state the ferryl compound I, which, once populated, shows substantial stability. Although our truncated active-site model system cannot assess the energetics associated with the proton-coupled electron transfer, **10** → **7**, in which a proton is supplied from outside, Zheng et al. reported this process to be essentially barrierless with an exothermicity of about 15 kcal mol⁻¹ with QM/MM calculations.^{47b} The model reaction **B** may be a possible pathway for avoiding the formation of the perferryl–oxo oxidant. Another important factor affecting the nature of compound I in the hybrid homolytic–heterolytic mechanism will be the extent of overlap between the radical orbital of the departing HO• and the orbital of the heme moiety from which an electron is removed, since the transition probability depends not only on the energy difference (thermodynamic driving force) but also on the electronic factor, which increases with overlap and decreases sharply with increasing distance between the two orbitals or decreasing overlap by symmetry. The evaluation of electronic coupling matrix elements in an actual biological system will be a very delicate problem, since the spin distribution is highly sensitive to the protein environment.^{40b,53} There can also be possibilities that a positive radical hole would be left on amino acid residues (e.g., tyrosines), as detected spectroscopically in substrate-free P450cam reactions with peroxy acetic acid,⁵⁴ and

that the formation of HO• may cause the oxidative modification of P450 and the degradation of the heme, as observed in the reconstituted CYP2B4 system⁵⁵ and in its F429H mutant.⁵⁶

In summary, the heterolysis of the FeO–OH₂ bond induced by the protonation of the distal oxygen of compound 0 (model reaction A) has a close affinity to the highly reactive perferryl–oxo oxidant, for which an extremely short lifetime is expected, 9 → 6 → 7* → 8*, while the alternative route initiated by the homolysis of the FeO–OH bond in compound 0 (model reaction B) could bypass the perferryl–oxo oxidant, 9 → 10 → 7 → 8, giving rise to the accumulation of ferryl compound I and thereby displaying a lifetime that may make this transient intermediate spectroscopically detectable. This interpretation suggests that the presence of two alternative pathways involving two active oxidants with very different reactivities could be a possible reason why compound I is too short-lived to be observed in the catalytic cycle of P450 (native pathway), while this is not the case in the reactions of P450 enzymes using peroxy acids such as *m*CPBA (shunt pathway);^{4a,b,d,16,19,20} i.e., the primary oxidizing species in the native reaction may be different from the one in the shunt reaction. The ratio of the homolytic and heterolytic cleavage of the O–O bond and associated product distributions were extensively studied for the shunt pathway in P450 reactions.⁵⁷ Although these are only a few theoretical aspects of the complex mechanistic problem, which may involve not only the low-spin states for the ferryl and perferryl species but also the intermediate- and high-spin multiradical states for the ferryl species via spin crossovers,^{17,18} our calculations can at least provide several possible mechanisms that we hope will stimulate further experimental and theoretical examinations.

4. CONCLUSIONS

We have performed hybrid DFT calculations on the reactivities of low-lying doublet and quartet ferryl–oxo oxidants and a doublet perferryl–oxo oxidant in the secondary hydrogen-atom abstraction from propane by compound I models (**1**, L = SCH₃[−] or SH[−]). The results clearly show the extremely high reactivity of the perferryl–oxo oxidant, ²I*, which lies in its unique bonding pattern as a mixed-valent resonance state bearing a pπ_O atomic oxygen radical, ↑Fe(V)=O ↔ ↑Fe(IV) •↑—↓•O.²¹ The activation barriers for hydrogen abstraction from propane by ²I* are only 2.0–2.5 kcal mol^{−1} (SCH₃ model) and 0.6–2.2 kcal mol^{−1} (SH model) in the gas phase, which are substantially smaller than those by the ferryl–oxo oxidants, ^{2,4}I [14.8–16.9 kcal mol^{−1} (SCH₃ model) and 13.4–17.8 kcal mol^{−1} (SH model)]. Even after considering the fact that the perferryl complex ²a* lies about 11–13 kcal mol^{−1} above the degenerate pair of the ground configurations, ^{2,4}a, total barriers are 12–15 kcal mol^{−1}, which is the smallest among the configurations considered by us. The perferryl species ²a* cuts through the ferryl surfaces for ^{2,4}a, providing a possible low-energy path for hydrogen abstraction. The above reactivity trends apply to both the gas and solution phase reactions, showing the same stability patterns of the TSs for hydrogen abstraction: ²TS1a* ≤ ⁴TS1a < ²TS1a < ²TS1a". The fact that a wide variety of density functionals (hybrid GGA, hybrid meta-GGA, and range-separated hybrid GGAs) give virtually the same qualitative trends puts particular confidence in our assertion that the perferryl–oxo oxidant is not only low lying but also much more reactive than the ferryl–oxo oxidant.

The behaviors of the doublet ferryl and perferryl oxidants during the O–O bond activation in precursor (protonated) compound 0 and in the subsequent C–H bond activation have also been addressed in the present study. Grid search using two parameters has been performed to explore the coupled O–O dissociation and hydrogen-atom transfer processes. The protonation state of the distal oxygen in compound 0 is found to make a difference in the hydroxylation mechanism. Considering the fact that ferryl and perferryl surfaces cross along heterolytic FeO–OH₂ bond elongation, we can reason that the distal oxygen protonation prior to the FeO–OH bond breaking might result in the preferential formation of the highly reactive perferryl–oxo oxidant, while proton-coupled electron transfer after the TS for homolytic FeO–OH bond breaking is surpassed might involve a stepwise process that occurs preferentially from the ferryl–oxo species. Of course, the actual reaction mechanism may be more complicated than the one we outline above. There should be a large number of possible reaction pathways thermally accessible, which are caused by multiple surface crossings among low-lying low-, intermediate- and high-spin states of the ferryl and perferryl species, depending on various subtle factors such as protein tertiary structure, ligand-field strength, redox potential of the heme, proton activity of environment, and so on. In this connection, the concerted pathway via the doublet perferryl species involves a key role of the motion of the thiolate ligand (asymmetric bond distortion along the O–Fe–S axis), which could make the suggested concerted mechanism competitive favorably with an electron-transfer event between the iron–oxo core and the ligands that converts the perferryl to ferryl compound I. This prediction is essentially independent of the particular choice of the ligand representation (SCH₃[−] or SH[−]). We anticipate that the presence of the ferryl and perferryl states of compound I with quite different reactivities should affect the amount of accumulation of compound I, thereby leading to various degrees of detection in the shunt pathway on the one hand^{4a,b,d,16,19,20} and elusiveness in the native P450 catalysis on the other hand. Undoubtedly, future QM/MM studies will continue to provide further information and insights difficult to obtain by experiments, and many more elaborate experimental studies can also be expected.

■ ASSOCIATED CONTENT

● Supporting Information

Twelve figures of natural orbitals, energy profiles, geometrical parameters, and solvent effects; nine tables of Mulliken charge and spin densities; and Cartesian coordinates, absolute energies, and $\langle S^2 \rangle$ values of optimized structures reported. This material is available free of charge via the Internet at <http://pubs.acs.org>.

■ AUTHOR INFORMATION

Corresponding Author

*E-mail: isobe@chem.sci.osaka-u.ac.jp.

Notes

The authors declare no competing financial interest.

■ ACKNOWLEDGMENTS

This study was performed through the “Development of Basic Technologies for Advanced Production Methods Using Microorganism Functions” project from the New Energy and Industrial Technology Development Organization (NEDO).

■ REFERENCES

- (1) (a) Sono, M.; Roach, M. P.; Coulter, E. D.; Dawson, J. H. *Chem. Rev.* **1996**, *96*, 2841–2888. (b) Guengerich, F. P. *Chem. Res. Toxicol.* **2001**, *14*, 611–650. (c) Meunier, B.; de Visser, S. P.; Shaik, S. *Chem. Rev.* **2004**, *104*, 3947–3980. (d) Denisov, I. G.; Makris, T. M.; Sligar, S. G.; Schlichting, I. *Chem. Rev.* **2005**, *105*, 2253–2278. (e) Ortiz de Montellano, P. R. *Chem. Rev.* **2010**, *110*, 932–948. (f) Omura, T.; Ishimura, Y.; Fujii-Kuriyama, Y., Eds. *Cytochrome P-450*, 2nd ed.; Kodansha: Tokyo, 1993. (g) Ortiz de Montellano, P. R., Ed. *Cytochrome P450: Structure, Mechanism, and Biochemistry*, 3rd ed.; Kluwer Academic/Plenum Publishers: New York, 2005. (h) Sigel, A.; Sigel, H.; Sigel, R. K. O., Eds. *The Ubiquitous Role of Cytochrome P450 Proteins In Metal Ions in Life Sciences*; John Wiley & Sons Ltd: Chichester, England, 2007; Vol. 3.
- (2) (a) Omura, T.; Sato, R. *J. Biol. Chem.* **1964**, *239*, 2370–2378. (b) Omura, T.; Sato, R. *J. Biol. Chem.* **1964**, *239*, 2379–2385.
- (3) (a) Schlichting, I.; Berendzen, J.; Chu, K.; Stock, A. M.; Maves, S. A.; Benson, D. E.; Sweet, R. M.; Ringe, D.; Petsko, G. A.; Sligar, S. G. *Science* **2000**, *287*, 1615–1622. (b) Davydov, R.; Makris, T. M.; Kofman, V.; Werst, D. E.; Sligar, S. G.; Hoffman, B. M. *J. Am. Chem. Soc.* **2001**, *123*, 1403–1415.
- (4) (a) Egawa, T.; Shimada, H.; Ishimura, Y. *Biochem. Biophys. Res. Commun.* **1994**, *201*, 1464–1469. (b) Kellner, D. G.; Hung, S.-C.; Weiss, K. E.; Sligar, S. G. *J. Biol. Chem.* **2002**, *277*, 9641–9644. (c) Dowers, T. S.; Rock, D. A.; Rock, D. A.; Jones, J. P. *J. Am. Chem. Soc.* **2004**, *126*, 8868–8869. (d) Spolitak, T.; Dawson, J. H.; Ballou, D. P. *J. Biol. Chem.* **2005**, *280*, 20300–20309.
- (5) (a) Groves, J. T.; McClusky, G. A. *J. Am. Chem. Soc.* **1976**, *98*, 859–861. (b) Groves, J. T.; McClusky, G. A.; White, R. E.; Coon, M. J. *Biochem. Biophys. Res. Commun.* **1978**, *81*, 154–160. (c) Groves, J. T. *J. Chem. Educ.* **1985**, *62*, 928–931. (d) Auclair, K.; Hu, Z.; Little, D. M.; Ortiz de Montellano, P. R.; Groves, J. T. *J. Am. Chem. Soc.* **2002**, *124*, 6020–6027.
- (6) (a) Hjelmeland, L. M.; Aronow, L.; Trudell, J. R. *Biochem. Biophys. Res. Commun.* **1977**, *76*, 541–549. (b) Gelb, M. H.; Heimbrook, D. C.; Mälkönen, P.; Sligar, S. G. *Biochemistry* **1982**, *21*, 370–377. (c) Miwa, G. T.; Walsh, J. S.; Lu, A. Y. H. *J. Biol. Chem.* **1984**, *259*, 3000–3004. (d) White, R. E.; Miller, J. P.; Favreau, L. V.; Bhattacharyya, A. *J. Am. Chem. Soc.* **1986**, *108*, 6024–6031. (e) Ortiz de Montellano, P. R.; Stearns, R. A. *J. Am. Chem. Soc.* **1987**, *109*, 3415–3420.
- (7) (a) Loew, G. H.; Harris, D. L. *Chem. Rev.* **2000**, *100*, 407–420. (b) Shaik, S.; Kumar, D.; de Visser, S. P.; Altun, A.; Thiel, W. *Chem. Rev.* **2005**, *105*, 2279–2328. (c) Shaik, S.; Cohen, S.; Wang, Y.; Chen, H.; Kumar, D.; Thiel, W. *Chem. Rev.* **2010**, *110*, 949–1017.
- (8) (a) Newcomb, M.; Toy, P. H. *Acc. Chem. Res.* **2000**, *33*, 449–455. (b) Nam, W.; Ryu, Y. O.; Song, W. J. *J. Biol. Inorg. Chem.* **2004**, *9*, 654–660. (c) Jin, S.; Bryson, T. A.; Dawson, J. H. *J. Biol. Inorg. Chem.* **2004**, *9*, 644–653.
- (9) (a) Vaz, A. D. N.; Permecky, S. J.; Raner, G. M.; Coon, M. J. *Proc. Natl. Acad. Sci. U.S.A.* **1996**, *93*, 4644–4648. (b) Vaz, A. D. N.; McGinnity, D. F.; Coon, M. J. *Proc. Natl. Acad. Sci. U.S.A.* **1998**, *95*, 3555–3560.
- (10) Jin, S.; Makris, T. M.; Bryson, T. A.; Sligar, S. G.; Dawson, J. H. *J. Am. Chem. Soc.* **2003**, *125*, 3406–3407.
- (11) (a) Park, M. J.; Lee, J.; Suh, Y.; Kim, J.; Nam, W. *J. Am. Chem. Soc.* **2006**, *128*, 2630–2634. (b) Seo, M. S.; Kamachi, T.; Kouno, T.; Murata, K.; Park, M. J.; Yoshizawa, K.; Nam, W. *Angew. Chem., Int. Ed.* **2007**, *46*, 2291–2294. (c) Franke, A.; Fertlinger, C.; van Eldik, R. *Angew. Chem., Int. Ed.* **2008**, *47*, 5238–5242.
- (12) (a) Ogliaro, F.; de Visser, S. P.; Cohen, S.; Sharma, P. K.; Shaik, S. *J. Am. Chem. Soc.* **2002**, *124*, 2806–2817. (b) Kamachi, T.; Shiota, Y.; Ohta, T.; Yoshizawa, K. *Bull. Chem. Soc. Jpn.* **2003**, *76*, 721–732.
- (13) (a) Newcomb, M.; Le Tadic-Biadatti, M.-H.; Chestney, D. L.; Roberts, E. S.; Hollenberg, P. F. *J. Am. Chem. Soc.* **1995**, *117*, 12085–12091. (b) Toy, P. H.; Newcomb, M.; Hollenberg, P. F. *J. Am. Chem. Soc.* **1998**, *120*, 7719–7729. (c) Newcomb, M.; Shen, R.; Choi, S. Y.; Toy, P. H.; Hollenberg, P. F.; Vaz, A. D. N.; Coon, M. J. *J. Am. Chem. Soc.* **2000**, *122*, 2677–2686.
- (14) Ogliaro, F.; Harris, N.; Cohen, S.; Filatov, M.; de Visser, S. P.; Shaik, S. *J. Am. Chem. Soc.* **2000**, *122*, 8977–8989.
- (15) (a) Newcomb, M.; Zhang, R.; Chandrasena, R. E.; Halgrimson, J. A.; Horner, J. H.; Makris, T. M.; Sligar, S. G. *J. Am. Chem. Soc.* **2006**, *128*, 4580–4581. (b) Sheng, X.; Horner, J. H.; Newcomb, M. *J. Am. Chem. Soc.* **2008**, *130*, 13310–13320. (c) Pan, Z.; Wang, Q.; Sheng, X.; Horner, J. H.; Newcomb, M. *J. Am. Chem. Soc.* **2009**, *131*, 2621–2628. (d) Sheng, X.; Zhang, H.; Im, S.-C.; Horner, J. H.; Waskell, L.; Hollenberg, P. F.; Newcomb, M. *J. Am. Chem. Soc.* **2009**, *131*, 2971–2976. (e) Wang, Q.; Sheng, X.; Horner, J. H.; Newcomb, M. *J. Am. Chem. Soc.* **2009**, *131*, 10629–10636.
- (16) Rittle, J.; Younker, J. M.; Green, M. T. *Inorg. Chem.* **2010**, *49*, 3610–3617.
- (17) (a) Chen, H.; Song, J.; Lai, W.; Wu, W.; Shaik, S. *J. Chem. Theory Comput.* **2010**, *6*, 940–953. (b) Randoń, M.; Broclawik, E.; Pierloot, K. *J. Chem. Theory Comput.* **2011**, *7*, 898–908.
- (18) Hirao, K.; Kumar, D.; Thiel, W.; Shaik, S. *J. Am. Chem. Soc.* **2005**, *127*, 13007–13018.
- (19) (a) Jung, C. *Biochim. Biophys. Acta* **2011**, *1814*, 46–57. (b) Jung, C.; de Vries, S.; Schünemann, V. *Arch. Biochem. Biophys.* **2011**, *507*, 44–55.
- (20) Rittle, J.; Green, M. T. *Science* **2010**, *330*, 933–937.
- (21) Isobe, H.; Yamanaka, S.; Okumura, M.; Yamaguchi, K.; Shimada, J. *J. Phys. Chem. B* **2011**, *115*, 10730–10738.
- (22) (a) Becke, A. D. *Phys. Rev. A* **1988**, *38*, 3098–3100. (b) Lee, C.; Yang, W.; Parr, R. G. *Phys. Rev. B* **1988**, *37*, 785–789. (c) Becke, A. D. *J. Chem. Phys.* **1993**, *98*, 5648–5652.
- (23) (a) Stevens, W. J.; Basch, H.; Krauss, M. *J. Chem. Phys.* **1984**, *81*, 6026–6033. (b) Stevens, W. J.; Krauss, M.; Basch, H.; Jasien, P. G. *Can. J. Chem.* **1992**, *70*, 612–630. (c) Cundari, T. R.; Stevens, W. J. *J. Chem. Phys.* **1993**, *98*, 5555–5565.
- (24) (a) Frisch, M. J.; Trucks, G. W.; Schlegel, H. B.; Scuseria, G. E.; Robb, M. A.; Cheeseman, J. R.; Montgomery, J. A., Jr.; Vreven, T.; Kudin, K. N.; Burant, J. C.; et al. *Gaussian 03*, revision E.01; Gaussian, Inc.: Wallingford, CT, 2004. (b) Frisch, M. J.; Trucks, G. W.; Schlegel, H. B.; Scuseria, G. E.; Robb, M. A.; Cheeseman, J. R.; Scalmani, G.; Barone, V.; Mennucci, B.; Petersson, G. A.; et al. *Gaussian 09*, revision B.01; Gaussian, Inc.: Wallingford, CT, 2010.
- (25) Wachters, A. J. H. *J. Chem. Phys.* **1970**, *52*, 1033–1036. (b) Bauschlicher, C. W., Jr.; Langhoff, S. R.; Barnes, L. A. *J. Chem. Phys.* **1989**, *91*, 2399–2411.
- (26) Hehre, W. J.; Radom, L.; Schleyer, P. v. R.; Pople, J. A. *Ab Initio Molecular Orbital Theory*; Wiley: New York, 1986.
- (27) (a) Barone, V.; Cossi, M. *J. Phys. Chem. A* **1998**, *102*, 1995–2001. (b) Cossi, M.; Rega, N.; Scalmani, G.; Barone, V. *J. Comput. Chem.* **2003**, *24*, 669–681.
- (28) Zhao, Y.; Truhlar, D. G. *Theor. Chem. Acc.* **2008**, *120*, 215–241.
- (29) Yanai, T.; Tew, D. P.; Handy, N. C. *Chem. Phys. Lett.* **2004**, *393*, 51–57.
- (30) (a) Heyd, J.; Scuseria, G. E.; Ernzerhof, M. *J. Chem. Phys.* **2003**, *118*, 8207–8215. (b) Heyd, J.; Scuseria, G. E. *J. Chem. Phys.* **2004**, *121*, 1187–1192. (c) Heyd, J.; Scuseria, G. E. *J. Chem. Phys.* **2006**, *124*, 219906.
- (31) Chai, J.-D.; Head-Gordon, M. *Phys. Chem. Chem. Phys.* **2008**, *10*, 6615–6620.
- (32) Löwdin, P.-O. *Phys. Rev.* **1955**, *97*, 1474–1489.
- (33) Harriman, J. E. *J. Chem. Phys.* **1964**, *40*, 2827–2839.
- (34) By using double quotation marks as “local triplet” and “local singlet”, we mean that they are quasi-classical spin arrangements ($\uparrow\uparrow$, $\downarrow\downarrow$, and $\uparrow\downarrow$), not quantum mechanical resonance states. We have used the prime symbol ('') or the double prime symbol (‘‘) to specify “local singlet” coupling between two electrons in the orthogonal π_{xz}^* and π_{yz}^* orbitals.
- (35) (a) Yamaguchi, K.; Takahara, Y.; Fueno, T. In *Applied Quantum Chemistry*; Smith, V. H., Jr., Scheafer, H. F., III, Morokuma, K., Eds.; D. Reidel: Boston, MA, 1986; pp 155–184. (b) Yamaguchi, K.; Jensen, F.; Dorigo, A.; Houk, K. N. *Chem. Phys. Lett.* **1988**, *149*, 537–542. (c) Yamaguchi, K.; Takahara, Y.; Fueno, T.; Houk, K. N. *Theor. Chim. Acta* **1988**, *73*, 337–364.

- (36) Löwdin, P.-O. *Phys. Rev.* **1955**, *97*, 1509–1520.
- (37) Shaik, S.; Filatov, M.; Schröder, D.; Schwartz, H. *Chem.—Eur. J.* **1998**, *4*, 193–199.
- (38) Note that, by definition (Figure 1), the constituent $p\pi_s$ orbital of HONO and LUNO for ${}^2\text{TS1}_{\perp}$ lies in the same plane containing the constituent π_{yz}^* orbital, while, in ${}^2\text{TS1}$, it lies in the nodal plane of the π_{yz}^* orbital.
- (39) (a) Fukui, K. *J. Phys. Chem.* **1970**, *74*, 4161–4163. (b) Fukui, K. *Acc. Chem. Res.* **1981**, *14*, 363–368. (c) Gonzalez, C.; Schlegel, H. B. *J. Phys. Chem.* **1990**, *94*, 5523–5527.
- (40) (a) There can also be another potential route for generating the ferryl–hydroxo species without the involvement of the perferryl–oxo oxidant. This is the direct electron transfer from the substrate to the heme with concomitant proton transfer. This mechanism can be operative if the substrate is an excellent electron donor.^{40b} (b) Wang, Y.; Chen, H.; Makino, M.; Shiro, Y.; Nagano, S.; Asamizu, S.; Onaka, H.; Shaik, S. *J. Am. Chem. Soc.* **2009**, *131*, 6748–6762.
- (41) (a) Borden, W. T. *J. Am. Chem. Soc.* **1975**, *97*, 5968–5970. (b) Kollmar, H.; Staemmler, V. *Theor. Chim. Acta* **1978**, *48*, 223–239.
- (42) (a) Olsen, L.; Rydberg, P.; Rod, T. H.; Ryde, U. *J. Med. Chem.* **2006**, *49*, 6489–6499. (b) Shaik, S.; Kumar, D.; de Visser, S. P. *J. Am. Chem. Soc.* **2008**, *130*, 10128–10140.
- (43) (a) Davydov, R.; Macdonald, I. D. G.; Makris, T. M.; Sligar, S. G.; Hoffman, B. M. *J. Am. Chem. Soc.* **1999**, *121*, 10654–10655. (b) Mak, P. J.; Denisov, I. G.; Victoria, D.; Makris, T. M.; Deng, T.; Sligar, S. G.; Kincaid, J. R. *J. Am. Chem. Soc.* **2007**, *129*, 6382–6383.
- (44) Poulos, T. L.; Kraut, J. *J. Biol. Chem.* **1980**, *255*, 8199–8205.
- (45) Dey, A.; Jiang, Y.; Ortiz de Montellano, P. R.; Hodgson, K. O.; Hedman, B.; Solomon, E. I. *J. Am. Chem. Soc.* **2009**, *131*, 7869–7878.
- (46) (a) Harris, D.; Loew, G.; Waskell, L. *J. Am. Chem. Soc.* **1998**, *120*, 4308–4318. (b) Hata, M.; Hirano, Y.; Hoshino, T.; Nishida, R.; Tsuda, M. *J. Phys. Chem. B* **2004**, *108*, 11189–11195. (c) Kamachi, T.; Yoshizawa, K. *J. Am. Chem. Soc.* **2003**, *125*, 4652–4661. (d) Guallar, V.; Friesner, R. A. *J. Am. Chem. Soc.* **2004**, *126*, 8501–8508.
- (47) (a) Kumar, D.; Hirao, H.; de Visser, S. P.; Zheng, J. J.; Wang, D.; Thiel, W.; Shaik, S. *J. Phys. Chem. B* **2005**, *109*, 19946–19951. (b) Zheng, J. J.; Wang, D.; Thiel, W.; Shaik, S. *J. Am. Chem. Soc.* **2006**, *128*, 13204–13215.
- (48) (a) Bach, R. D.; Dmitrenko, O. *J. Am. Chem. Soc.* **2006**, *128*, 1474–1488. (b) Bach, R. D. *J. Phys. Chem. A* **2010**, *114*, 9319–9332.
- (49) Atkins, W. M.; Sligar, S. G. *J. Biol. Chem.* **1988**, *263*, 18842–18849.
- (50) (a) Altun, A.; Guallar, V.; Friesner, R. A.; Shaik, S.; Thiel, W. *J. Am. Chem. Soc.* **2006**, *128*, 3924–3925. (b) Altun, A.; Shaik, S.; Thiel, W. *J. Comput. Chem.* **2006**, *27*, 1324–1337. (c) Altun, A.; Shaik, S.; Thiel, W. *J. Am. Chem. Soc.* **2007**, *129*, 8978–8987. (d) Kumar, D.; Altun, A.; Shaik, S.; Thiel, W. *Faraday Discuss.* **2011**, *148*, 373–383.
- (51) Chen, H.; Hirao, H.; Derat, E.; Schlichting, I.; Shaik, S. *J. Phys. Chem. B* **2008**, *112*, 9490–9500.
- (52) (a) Groves, J. T.; Gross, Z.; Stern, M. K. *Inorg. Chem.* **1994**, *33*, 5065–5072. (b) Nam, W.; Lee, H. J.; Oh, S.-Y.; Kim, C.; Jang, H. G. *J. Inorg. Biochem.* **2000**, *80*, 219–225. (c) Nam, W.; Park, S.-E.; Lim, I. K.; Lim, M. H.; Hong, J.; Kim, J. *J. Am. Chem. Soc.* **2003**, *125*, 14674–14675.
- (53) (a) Ogliaro, F.; Cohen, S.; Filatov, M.; Harris, N.; Shaik, S. *Angew. Chem., Int. Ed.* **2000**, *39*, 3851–3855. (b) Ogliaro, F.; de Visser, S. P.; Groves, J. T.; Shaik, S. *Angew. Chem., Int. Ed.* **2001**, *40*, 2874–2878.
- (54) (a) Schünemann, V.; Jung, C.; Trautwein, A. X.; Mandon, D.; Weiss, R. *FEBS Lett.* **2000**, *479*, 149–154. (b) Schünemann, V.; Jung, C.; Terner, J.; Trautwein, A. X.; Weiss, R. *J. Inorg. Biochem.* **2002**, *91*, 586–596. (c) Schünemann, V.; Lendzian, F.; Jung, C.; Contzen, J.; Barra, A.-L.; Sligar, S. G.; Trautwein, A. X. *J. Biol. Chem.* **2004**, *279*, 10919–10930.
- (55) Karuzina, I. I.; Zgoda, V. G.; Kuznetsova, G. P.; Samenkova, N. F.; Archakov, A. I. *Free Radical Biol. Med.* **1999**, *26*, 620–632.
- (56) (a) Davydov, R.; Razeghifard, R.; Im, S.-C.; Waskell, L.; Hoffman, B. M. *Biochemistry* **2008**, *47*, 9661–9666. (b) Hamdane, D.; Xia, C.; Im, S.-C.; Zhang, H.; Kim, J.-J. P.; Waskell, L. *J. Biol. Chem.* **2009**, *284*, 11374–11384. (c) Usharani, D.; Zazza, C.; Lai, W.; Chourasia, M.; Waskell, L.; Shaik, S. *J. Am. Chem. Soc.* **2012**, *134*, 4053–4056.
- (57) (a) White, R. F.; Sligar, S. G.; Coon, M. J. *J. Biol. Chem.* **1980**, *255*, 11108–11111. (b) Shimizu, T.; Murakami, Y.; Hatano, M. *J. Biol. Chem.* **1994**, *269*, 13296–13304. (c) Correia, M. A.; Yao, K.; Allentoff, A. J.; Wrighton, S. A.; Thompson, J. A. *Arch. Biochem. Biophys.* **1995**, *317*, 471–478. (d) Barr, D. P.; Martin, M. V.; Guengerich, F. P.; Mason, R. P. *Chem. Res. Toxicol.* **1996**, *9*, 318–325. (e) Kuo, C.-L.; Raner, G. M.; Vaz, A. D. N.; Coon, M. J. *Biochemistry* **1999**, *38*, 10511–10518.